

12-15-2018

Studies of Inner-Shell Chemistry of Mercury Based Compounds at Extreme Conditions

Sarah Schyck
s.schyck@gmail.com

Follow this and additional works at: <https://digitalscholarship.unlv.edu/thesesdissertations>



Part of the [Physics Commons](#)

Repository Citation

Schyck, Sarah, "Studies of Inner-Shell Chemistry of Mercury Based Compounds at Extreme Conditions" (2018). *UNLV Theses, Dissertations, Professional Papers, and Capstones*. 3453.
<https://digitalscholarship.unlv.edu/thesesdissertations/3453>

This Thesis is protected by copyright and/or related rights. It has been brought to you by Digital Scholarship@UNLV with permission from the rights-holder(s). You are free to use this Thesis in any way that is permitted by the copyright and related rights legislation that applies to your use. For other uses you need to obtain permission from the rights-holder(s) directly, unless additional rights are indicated by a Creative Commons license in the record and/or on the work itself.

This Thesis has been accepted for inclusion in UNLV Theses, Dissertations, Professional Papers, and Capstones by an authorized administrator of Digital Scholarship@UNLV. For more information, please contact digitalscholarship@unlv.edu.

STUDIES OF INNER-SHELL CHEMISTRY OF MERCURY BASED
COMPOUNDS UNDER EXTREME
CONDITIONS

By

Sarah Schyck

Bachelor of Science in Physics
University of Georgia
2015

A thesis submitted in partial fulfillment
of the requirements for the

Master of Science - Physics

Department of Physics and Astronomy
College of Sciences
The Graduate College

University of Nevada, Las Vegas
December 2018



Thesis Approval

The Graduate College
The University of Nevada, Las Vegas

November 19, 2018

This thesis prepared by

Sarah Schyck

entitled

Studies of Inner-Shell Chemistry of Mercury Based Compounds under Extreme Conditions

is approved in partial fulfillment of the requirements for the degree of

Master of Science - Physics
Department of Physics and Astronomy

Michael Pravica, Ph. D.
Examination Committee Chair

Kathryn Hausbeck Korgan, Ph.D.
Graduate College Interim Dean

Eunja Kim, Ph. D.
Examination Committee Member

Stephen Lepp, Ph. D.
Examination Committee Member

David Hatchett, Ph. D.
Graduate College Faculty Representative

ABSTRACT

STUDIES OF INNER-SHELL CHEMISTRY OF MERCURY BASED COMPOUNDS UNDER EXTREME CONDITIONS

by

Sarah Schyck

Prof. Michael Pravica, Defense Committee Chair

University of Nevada, Las Vegas

It has been theoretically predicted that when mercury difluoride (HgF_2) is pressurized to above 50 GPa in the presence of molecular fluorine, it will most likely transform into mercury tetrafluoride (HgF_4), thus mercury will behave as a transition element at high pressure. However, there is no experimental evidence verifying this prediction yet. To begin with, the crystalline properties of pure HgF_2 at high pressure were not experimentally established. In this thesis, the high pressure structural properties of HgF_2 are investigated by means of synchrotron X-ray powder diffraction. Our results reveal that the predicted, ambient cubic structure of HgF_2 with the space group $Fm\bar{3}m$, can be obtained via a high-pressure ramp purification process using powdered HgF_2 mixed with crystalline XeF_2 which serves as our molecular fluorine source. The structural transformation of purified HgF_2 is observed above 2.5 GPa, and by using first-principle calculations, two candidate structures with space groups $Pnma$ and $Pnam$ are proposed which persist up to 63 GPa. Furthermore, studies of HgF_2 in the presence of F_2 produced by the X-ray induced decomposition of XeF_2 up to 70 GPa are reviewed. The obtained results provide more insights into the high-pressure behavior of mercury-fluorine compounds and will benefit further experimental investigation of high pressure induced synthesis of HgF_4 .

ACKNOWLEDGMENTS

I want to express my gratitude to my supervisor for his professional guidance during this thesis project. Specifically, thank you Professor Michael Pravica for providing me the opportunity to complete this master's thesis in his research group. I would also like to thank Dr. Eunja Kim for her ideas and discussions during these years.

I am grateful to the other official committee members of this thesis, Professor Stephen Lepp and Professor David Hatchett, for their encouraging comments and professional review.

I would like to express my appreciation to all my co-authors for their contributions to these studies. Particularly, I want to thank Dr. Egor Evlyukhin for his endless help in analyses and support during my thesis project.

I want to acknowledge the staff of Argonne National Laboratories, HPCAT Sector 16 and the Canadian Light Source for their help during this project.

For financial support, I gratefully acknowledge support from the Department of Energy National Nuclear Security Administration (DOE-NNSA) under Award Number DE-NA0002912. I also acknowledge support from the DOE Cooperative Agreement No. DE-FC08-01NV14049 with the University of Nevada, Las Vegas.

I am grateful to my parents, Erin and Michael Schyck, and my brother, Mikey, for their continuous support, inspiration, and love throughout my life.

TABLE OF CONTENTS

ABSTRACT.....	ii
ACKNOWLEDGMENTS	iii
LIST OF TABLES.....	v
LIST OF FIGURES	vi
CHAPTER 1 : INTRODUCTION.....	1
CHAPTER 2 : EXPERIMENTAL AND THEORETICAL BACKGROUND.....	3
A. X-ray's Interaction with Matter	3
B. Experimental and theoretical background of HgF ₄ synthesis	5
CHAPTER 3 : EXPERIMENTAL SETUPS AND CHARACTERIZATION METHODS.....	6
A. Diamond Anvil Cell.....	6
B. Ruby as a pressure marker	8
C. Infrared Spectroscopy	9
D. X-ray diffraction	12
E. X-ray absorption spectroscopy.....	15
F. Raman spectroscopy	17
CHAPTER 4 : STRUCTURAL PROPERTIES OF HgF ₂ AT HIGH PRESSURE	20
A. Purification of HgF ₂ by high pressure ramp process	20
B. HgF ₂ at high pressures	23
CHAPTER 5 : INVESTIGATION OF HgF ₄ AT HIGH PRESSURE.....	32
A. XRD characterization of irradiated HgF ₂ XeF ₂ samples.....	33
B. XRD characterization of unirradiated HgF ₂ XeF ₂ samples.....	39
C. IR characterization of irradiated HgF ₂ XeF ₂ samples	43
D. Characterization of HgF ₂ XeF ₂ samples by XAS	44
E. X-ray induced decomposition of XeF ₂	46
CHAPTER 6 : CONCLUSIONS	48
CHAPTER 7 : FUTURE WORK	49
REFERENCES	50
CURRICULUM VITAE.....	60

LIST OF TABLES

<i>Table 3-1</i> Features of the CLS Far-IR beamline.....	12
<i>Table 3-2</i> Characteristic excitation and fluorescence energies of Mercury[51]......	16
<i>Table 4-1</i> Observed and calculated d spacings for the fluorite-type phase of HgF_2 at 0 GPa. These peaks are fit to an cubic unit cell with $a = 5.5327 \text{ \AA}$ and $V=169.367 \text{ \AA}^3$	24
<i>Table 4-2</i> Equation of state parameters for HgF_2 . Asterisk (*) represents fixed values.....	25
<i>Table 4-3</i> Observed and calculated d spacings for the cotunnite-type phase of HgF_2 at 5.6 GPa. The peaks are fit to a orthorhombic unit cell with $a = 5.7678 \text{ \AA}$, $b = 3.5334 \text{ \AA}$, $c = 7.1388 \text{ \AA}$, and $V= 145.490 \text{ \AA}^3$	28
<i>Table 4-4</i> Predicted lattice parameters and atomic positions of two candidate orthorhombic HgF_2 phases at around 6 GPa. The Pnam phase is the orthorhombic cotunnite-type PbCl_2 structure...	29
<i>Table 5-1</i> Assignment of XeF_2 peaks based on [65].....	47

LIST OF FIGURES

Figure 2-1. Electronic relaxation processes triggered by X-ray absorption.	4
Figure 3-1 Schematic of a diamond anvil cell shown with a gasket.....	7
Figure 3-2 An example of a ruby fluorescence shift with pressure (Reprint from [36])	8
Figure 3-3 Bending and stretching vibrations (Reprint from [28]).....	10
Figure 3-4 The basic physical process for X-ray absorption spectroscopy.	15
Figure 3-5 Various features in the XANES region (Redraw from [51]).	17
Figure 4-1 Characterization of structural properties of initial HgF ₂	21
Figure 4-3 XRD patterns of purification steps.	21
Figure 4-4 XRD patterns of HgF ₂ at selected pressure points up to 2.5 GPa..	24
Figure 4-5 XRD patterns of HgF ₂ at selected pressure points.....	26
Figure 4-6 XRD patterns of the experimentally obtained at 6.8 GPa and theoretically predicted orthorhombic crystal structures with the space groups Pnam and Pnma.....	27
Figure 4-7 Lattice parameters of the cotunnite-type phase of HgF ₂	28
Figure 4-8 Interplanar spacing difference over the studied pressure range (fluorite-type to cotunnite-type phases) for HgF ₂	29
Figure 4-9 Pressure vs. volume data over the whole pressure range for the experimental (black curve) and the theoretical (red curve) data.	30
Figure 5-1 Pictures of HgF ₂ and XeF ₂ mixture at high pressure	33
Figure 5-2 X-ray produced 2-D map of irradiated HgF ₂ XeF ₂ sample.....	33
Figure 5-3 XRD patterns of: “average area”.....	34
Figure 5-4 XRD patterns of: “dark area” in the irradiated HgF ₂ XeF ₂	35
Figure 5-5 XRD patterns of: “bright area middle” in the irradiated HgF ₂ XeF ₂ sample.....	36
Figure 5-6 XRD patterns of: “bright area edge” in the irradiated HgF ₂ XeF ₂ sample.....	37

Figure 5-7 XRD patterns comparison of different areas in the irradiated sample.	38
Figure 5-8 X-ray produced 2-D map of unirradiated HgF ₂ XeF ₂ sample.....	39
Figure 5-9 XRD patterns of: “dark area” in the unirradiated HgF ₂ XeF ₂ sample.....	40
Figure 5-10 XRD patterns of: “middle area” in the unirradiated HgF ₂ XeF ₂ sample.....	41
Figure 5-11 XRD patterns comparison of different areas in the unirradiated HgF ₂ XeF ₂ sample obtained at 50 GPa.	42
Figure 5-12 Far-IR of the irradiated sample of HgF ₂ XeF ₂ :	43
Figure 5-13 X-ray absorption spectra of samples.	45
Figure 5-14 Raman spectra at selected pressure points	46
Figure 5-15 Raman spectra of selected pressure points.....	47

CHAPTER 1: INTRODUCTION

Generally, at ambient conditions chemical bonds between atoms form by exchanging their valence electrons, whereas all core electrons remain inert[1]. Only recently, chemists who study high pressure suggested the possibility that inner-shell electrons may interact with neighboring atoms with unoccupied outer-shell orbitals at high pressure, thereby enabling the formation of novel chemical structures and chemical bonding which are different from those at ambient conditions[2]. Indeed, at high pressure the chemical changes of elements are largely due to the relative shifts and broadening of the electron energy levels/orbitals due to decreasing interatomic distances and typically an increase of pressure leads to an increase of energy of electronic orbitals. However, depending on the electronic states and shapes of the orbitals the energy shifts can vary. For instance, the 4s orbital of Ni, which is metallic at ambient conditions, increases faster in energy with an increase of pressure than the 3d orbital and, hence, at a certain pressure the 3d orbital becomes lower in energy than the 4s orbital. Due to these energy changes of electronic orbitals, Ni becomes an insulator at high pressure[3].

The orbitals energetic displacement may also occur in different atoms under high pressure[4]. For instance, it has been theoretically demonstrated that at high pressure the Cs 5p orbital is higher in energy than the F 2p orbital (which is opposite from ambient pressure conditions), thereby enabling the inner-shell 5p electrons of Cs to couple with F atoms and form Cs-F covalent bonds[2]. Several CsF_n compounds at high pressure were predicted and it was demonstrated that when the oxidation state of Cs is greater than +1 it behaves as a *p*-block element[5]. Moreover, it has been proposed that high pressure techniques can also be used to prepare unusual oxidation states of Hg-based compounds[6]. At ambient conditions, the highest oxidation state of mercury is +2 and it is considered as a post-transition metal[7]. However, it has

been theoretically predicted that when HgF_2 is pressurized above 50 GPa in the presence of F_2 molecules, it may transform into HgF_4 and at pressures higher than 73 GPa into HgF_3 [6]. Nevertheless, this theoretical prediction has not been experimentally verified yet and furthermore, the crystalline properties of pure HgF_2 at high pressure were not experimentally established. The goal of my studies entails an investigation of the high pressure behavior of HgF_2 and then to seek to produce HgF_4 by creating an environment rich in molecular fluorine in a diamond anvil cell (DAC) by irradiating a mixture of HgF_2 and XeF_2 . The manuscript is organized as follows.

Chapter II presents a brief description of the theoretical and experimental background on the interaction of X-ray's with matter. Additionally, the previous efforts of HgF_4 synthesis are discussed.

Chapter III is devoted to a detailed presentation of the characterization methods and experimental setups of: infrared (IR) spectroscopy, X-ray diffraction (XRD), and descriptions of the beamlines used in this work.

Chapter IV describes the purification method of HgF_2 via a high pressure ramp process. Moreover, the experimental investigations of the high pressure induced structural behavior of HgF_2 by means of XRD are discussed.

Chapter V is focused on the experimental attempts of HgF_4 synthesis via X-ray induced decomposition of powdered HgF_2 and crystalline xenon difluoride (XeF_2) mixture. The HgF_4 fabrication process is investigated by IR spectroscopy and synchrotron XRD.

The last chapter summarizes the main results of this master's thesis.

CHAPTER 2: EXPERIMENTAL AND THEORETICAL BACKGROUND

A. X-ray's Interaction with Matter

The main factors that cause damage due to X-ray radiation, are the electronic excitation of atoms and molecules and following relaxation processes [8–13]. Recent progress in understanding these events that lead to X-ray radiation induced damage has been demonstrated by investigations of electronic decay processes induced by radiation in loosely bound chemical systems [8,14–18]. Essentially, a K-shell electron is excited to a bound state by the absorption of a sufficiently energetic X-ray photon [9,10] or the electron is removed (ionized) from the host into the continuum initiating a cascade of relaxation processes. The environment and chemical composition of the system after irradiation affects the origin and sequence of the relaxation processes [17,19–21]. Recently, a theoretical study investigated the role of metal ions in X-ray-induced photochemistry [8]. It has been shown that absorption of X-rays by micro solvated Mg^{2+} results in cascade of ultrafast electronic relaxation steps that include both intra- and inter-molecular processes. At the end of this cascade, the metal ion reverts to its original oxidation state whereas the surrounding environment becomes multiply ionized and contains many radicals and slow electrons. Such high capability of chemical systems to absorb X-ray photons which leads to distortion of molecular structure makes the study of these compounds using X-ray crystallographic techniques problematic. Thus, understanding the mechanisms of X-ray induced damage and the possibility to control this damage will be extremely useful for: (i) understanding the response of chemical systems to ionizing radiation, (ii) development of novel synthetic methods to create unique and potentially useful materials, and (iii) enabling more accurate analysis of their properties.

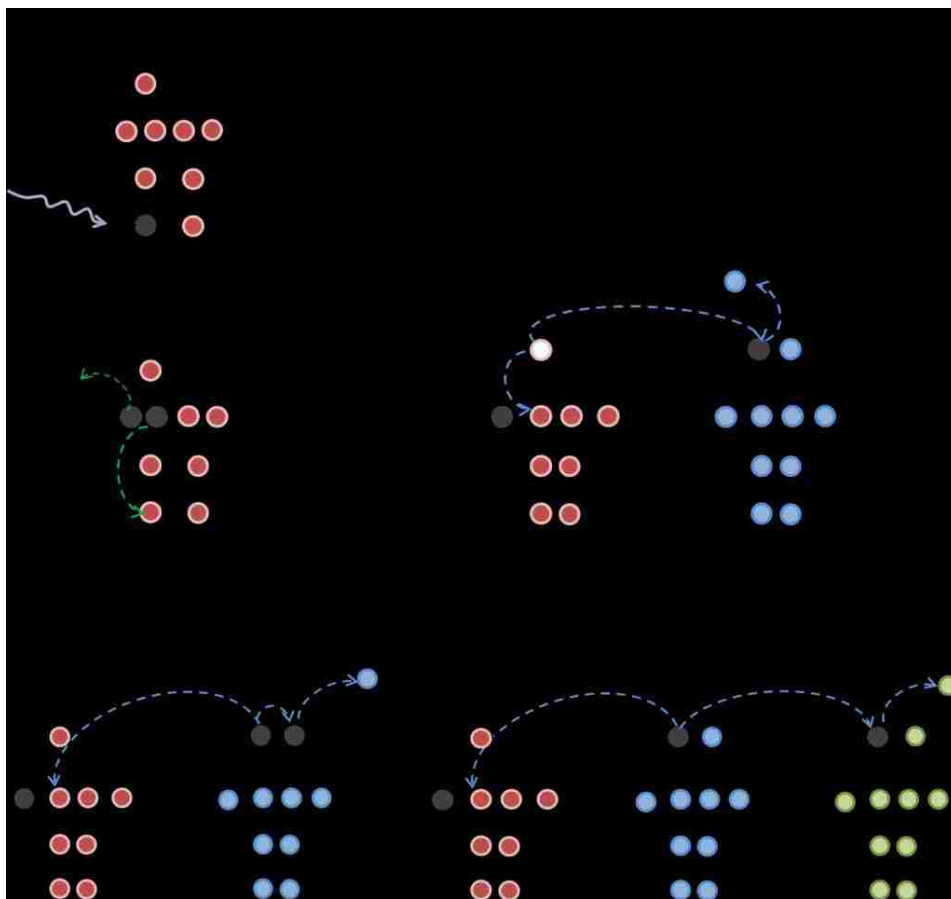


Figure 0-1. Electronic relaxation processes triggered by X-ray absorption.

It should also be noted that complex molecules (including organic molecules) have been found in outer space[22] and many fundamental questions remain pertaining to how these compounds were synthesized over billions of years in or on comets, asteroids, planets, or in the empty interstellar medium. Recently, we have demonstrated that X-rays with energies near the K-edge can be particularly effective in enabling chemical decomposition[23] and concomitant synthesis6 including synthesis of a novel form of doped solid carbon monoxide[24]. As many biomolecules are polymers, one question that begs to be answered pertains to the probable role of X-rays in the synthesis of organic precursors (such as oxalate salts [25]).

B. Experimental and theoretical background of HgF₄ synthesis

Chemical elements from group 12 in the periodic table, which include Hg, are considered to be post-transition metals due to their ability to be oxidized in the +2 state. Nevertheless, it has been predicted that Hg could be oxidized to higher oxidation states because of the large relativistic orbital electron effects that perturb the 5d energies[2]. Recently, several experimental and theoretical attempts to study Hg in a higher oxidation state have been made. Namely, by applying quantum chemical calculations, metastable, gas-phase planar molecules containing Hg(+4) have been suggested[26]. HgF₄ molecules have also been detected from the photochemical reaction of Hg and F₂ in solid neon and argon at 4 K using matrix-isolation infrared (IR) spectroscopy[27]. However, the authors of [28] demonstrated that previous experimental detection of HgF₄ molecules in solid neon matrices was not convincing due to the misassignment of the HgF₄ vibrational stretching modes and the high noise level. Concerning Hg in oxidation state +3: (i) HgF₃ in molecular form has been theoretically predicted [29] and (ii) experimentally demonstrated in a short-lived compound[30]. All these examples clearly show the potential ability of Hg to behave as a transition metal in the presence of strong oxidizing agents, such as fluorine. Additionally, Botana et al. have found that high pressure can be used as a practical tool to stabilize Hg in both +3 and +4 oxidation states[6]. Nevertheless, thermodynamically stable HgF₄ has not been experimentally observed as far as we are aware and; therefore, the high pressure induced synthesis of HgF₄ has been the primary focus in this work.

CHAPTER 3: EXPERIMENTAL SETUPS AND CHARACTERIZATION METHODS

A. Diamond Anvil Cell

Extremely high static pressure, up to 770 GPa [31], can be generated using a diamond anvil cell (DAC). A typical schematic of a DAC is displayed in Fig. 3-1. A metal gasket, consisting of rhenium-based or stainless-steel, is preindented/squeezed between two diamond anvil culets and a small hole is drilled to act as the sample confining chamber. The pressure, the force applied per unit area, that a DAC can ultimately achieve depends on (i) the dimensions of the diamond culets, (ii) the sample chamber size (diameter and thickness), and (iii) the yield strength of the gasket material.

Diamonds as anvils are convenient for X-ray analyses due to their transparency to hard X-rays with energies (typically greater than 7keV) that are commonly used for crystal structure determination [32]. In the experiments presented in this thesis, the diameter of the culet face on the diamond anvil is in the range 300-400 μm which allowed for pressures to be generated up to at least 60 GPa.

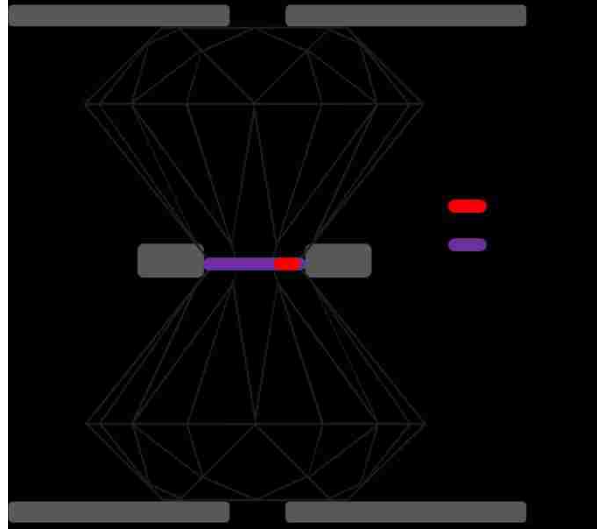


Figure 0-1 Schematic of a diamond anvil cell shown with a gasket used for sample containment.

An important component of a DAC is the metal gasket that acts as the sample chamber and a protective barrier between the two diamond faces[33]. In these experiments, a rhenium-based gasket was used and prepared by these two steps: indentation of the gasket and drilling a circular hole to $\geq 100 \mu\text{m}$ by spark erosion electrical discharge machining (EDM) or laser micro-machining. The prepared gasket is aligned on the culet face of the diamond where the sample and the pressure markers (ruby spheres) are manually loaded into the opening.

In these experiments, a symmetric style diamond anvil cell (DAC) was used for sample pressurization (up to 63 GPa). The DAC had a culet face of $300 \mu\text{m}$ in diameter. Rhenium gaskets were pre-indented to about $40 \mu\text{m}$ thickness, and they were subsequently drilled to $80 \mu\text{m}$ diameter using the laser micro-machining system [34] situated at the High-Pressure Collaborative Access Team's facility (HP-CAT) located in the Advanced Photon Source of Argonne National Laboratory (APS-ANL). All loading procedures of HgF_2 (Sigma-Aldrich 97% purity), were completed in an inert gas backfilled atmosphere glovebox due to the material's high moisture

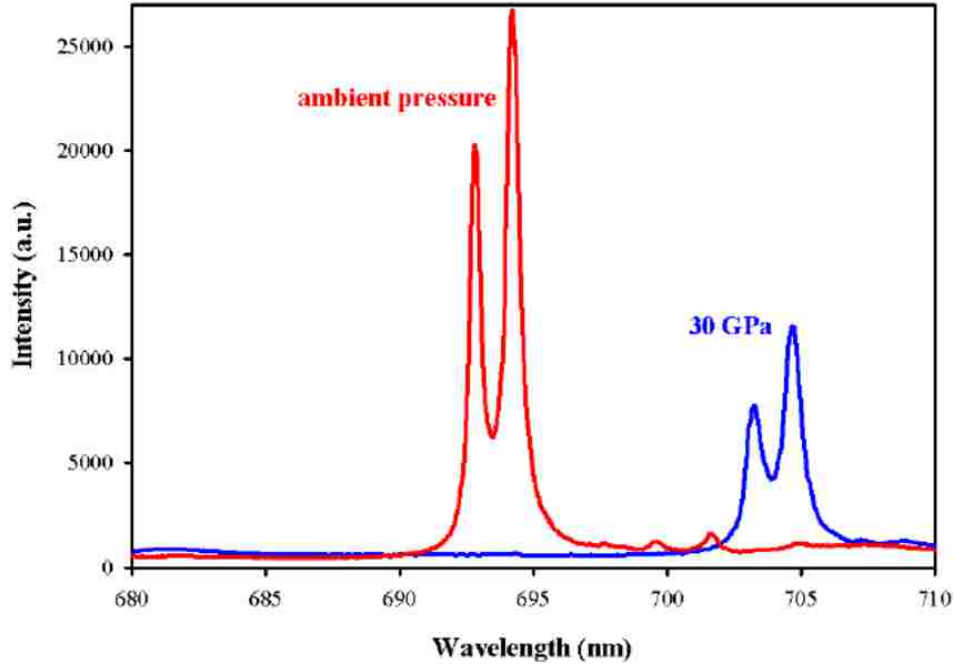


Figure 0-2 An example of a ruby fluorescence shift with pressure (Reprint from [36])

sensitivity. HgF_2 powder samples were loaded into a DAC along with a ruby sphere for pressure measurements [35] and XeF_2 (Sigma-Aldrich 99.99%). No pressure transmitting medium was used in our experiments.

B. Ruby as a pressure marker

The typical method to determine pressure inside a diamond anvil cell is based on the ruby fluorescence line shift. When a ruby ($\text{Al}_2\text{O}_3:\text{Cr}^{2+}$) sphere undergoes a pressure change, the two strong fluorescence lines (R1 and R2) shift in energy [36]. The pressure that is based on the fluorescence shift of ruby is defined by:

$$P = \frac{1904}{7.715} \left(\frac{\lambda}{\lambda_0}^{7.715} - 1 \right)$$

where λ is the shift of wavelength from ambient conditions and λ_0 is the wavelength of the ruby R1 fluorescence line [37].

Fig. 3-2 displays some ruby fluorescence spectra excited by 632 nm laser irradiation at ambient conditions and at 30 GPa. In situ ruby pressure shifts were measured using an ISA HR460® spectrometer with a Peltier-cooled CCD detector (Andor® 1024x128 pixels). An Ar ion multiline laser tuned to 532 nm served as the excitation source.

C. Infrared Spectroscopy

Infrared (IR) spectroscopy is a technique based on the absorption of IR radiation on the chemical bonds of molecules and the resulting vibrations of the atoms. The typical wavelength, λ , of IR radiation ranges from 780 nm to 1000 μm which is split into three regions: (i) Near-IR (780 nm to 2500 nm), (ii) Mid-IR (2.5 μm to 25 μm), and (iii) Far-IR (25 μm to 1000 μm)[38]. In IR spectroscopy, the convention is to use the reciprocal of wavelength, the *wavenumber* (cm^{-1})[39], which is defined as:

$$\tilde{\nu} = \frac{1}{\lambda} = \frac{\nu}{c} \quad (3-1)$$

where ν is the frequency of radiation and c is the speed of light in a vacuum.

IR radiation has sufficient energy to alter the vibrational and rotational states of a molecule. This energy[39] is defined as:

$$E = h\nu = hc\tilde{\nu} \quad (3-2)$$

where h is Planck's constant. Molecular vibrations are due to the change in bond length or bond angle, stretching and bending, respectively (see Fig. 3-1[40]). Stretching vibrations can be further classified as either symmetric (in-phase) or asymmetric (out-of-phase).

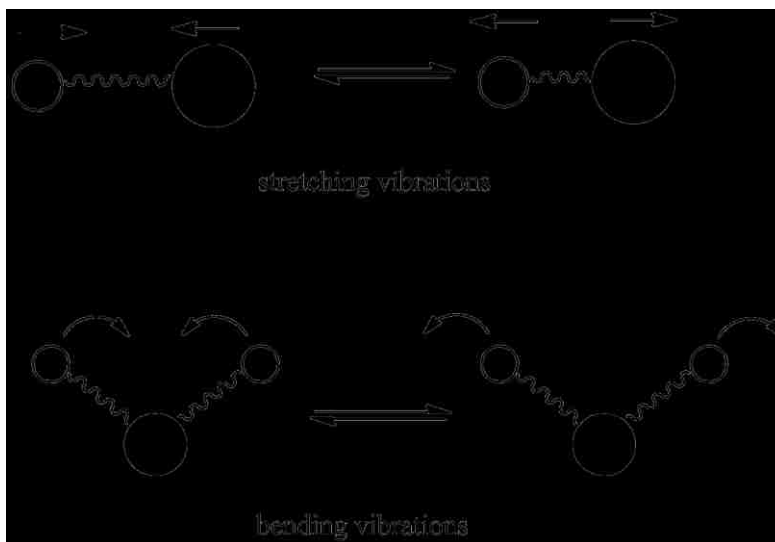


Figure 0-3 Bending and stretching vibrations (Reprint from [28]).

There are two requirements for a molecule to absorb IR radiation: (i) the IR radiation energy must be equal to the difference in energy of the ground state and the excited state of a molecule and (ii) a change in the dipole moment of the molecule due to molecular vibrations.

The dipole moment, μ , for a molecule:

$$\vec{\mu} = \sum e_i \vec{r}_i \quad (3-3)$$

where e_i is the charge magnitude and r_i represents the vector positions of the atomic charges[41]. For example, a homonuclear diatomic molecule, such as O_2 , has no dipole moment and is IR inactive. Whereas, a heteronuclear diatomic molecule, such as HCl, has a dipole moment and is IR active.

A typical experiment with IR spectroscopy is completed in transmission setup where IR radiation passes through a sample and the energy losses at various wavelengths are recorded by a

detector. Transmittance is defined as the ratio of the transmitted IR radiation $I(\tilde{\nu})$ to the incident intensity $I_0(\tilde{\nu})$:

$$T(\tilde{\nu}) = \frac{I(\tilde{\nu})}{I_0(\tilde{\nu})} \quad (3-4)$$

However, the absorbance is used to describe the obtained data, and the absorbance is related to the transmittance by:

$$A(\tilde{\nu}) = \ln \frac{1}{T} \quad (3-5)$$

More commonly known as the Beer-Lambert's Law:

$$A(\tilde{\nu}) = \alpha \tilde{\nu} l n \quad (3-6)$$

where α is the molecular absorption coefficient, l is the path length, and n is the concentration of the molecule.

For a synchrotron Fourier transform IR (FTIR) spectrometer, IR radiation is generated from a synchrotron source which travels through a beam splitter that reflects half of the light into a static mirror and half into a movable mirror. IR radiation that is reflected from both mirrors encounters interference back at the beam splitter. This beam then passes through the sample, and an interferogram is collected by the detector. The IR absorption spectrum is calculated from the Fourier transform of the interferogram.

IR spectroscopic measurements in this work were carried out at the Canadian Light Source (CLS) Far-IR beamline *in situ* inside the diamond anvil cell (DAC) for samples under compression. Far-IR studies were performed on the samples at the 02B1-1 beamline at the CLS. The collection

optics and DAC were housed in front of the Fourier Transform (FT)-IR system with a plexiglass enclosure, and it was continuously purged from water vapor (as measured with a humidity sensor) using positive pressure nitrogen blowoff gas from a nearby liquid N₂ dewar. A Horizontal Microscope system collected Far-IR spectra. The IR beam was redirected from the sample compartment of a Bruker IFS 125 HR[®] spectrometer [®] to within the working distance of a Schwarzschild objective which focused IR light onto the sample. A similar objective behind the sample collected the transmitted light and directed it onto an off-axis parabolic mirror which refocused the light into a low temperature Si Bolometer detector. The spectrometer was equipped with a 6 μm mylar beamsplitter, and the data were collected using a scanner velocity of 40 kHz, 12.5 mm entrance aperture, and a resolution of 1 cm⁻¹. The Si Bolometer detector was set for 16× gain. The interferograms were transformed using a zero filling factor of 8 and a 3-term Blackman Harris apodization function. (see Table 3-1). IR spectroscopy was utilized rather than Raman due to irradiated samples tendency to be highly fluorescent after exposure to an X-ray beam.

Table 0-1 Features of the CLS Far-IR beamline

<i>Far-IR Feature</i>	Description
<i>Source</i>	Synchrotron (Bending Magnet)
<i>Detector</i>	Si Bolometer
<i>Region</i>	35-650 cm ⁻¹
<i>Flux (V/s/0.1%BW) @ 100 mA</i>	1 x 10 ¹³ @ 100 μm
<i>Resolution Δ E</i>	≥ 0.001 cm ⁻¹

D. X-ray diffraction

For X-ray diffraction (XRD), hard X-rays on the range of a 20 to 0.1 Å are utilized as this range is comparable to atomic distances. Hard X-rays can then effectively probe the structural arrangement of atoms and molecules in materials. The two main sources to generate X-rays are either X-ray tubes or synchrotron radiation. In an X-ray tube, electrons are accelerated under a

high-voltage towards a target. When the electrons encounter the target, deceleration radiation occurs which is the production of electromagnetic radiation through the deceleration of an electron by an atomic nucleus[42]. In a synchrotron, X-rays are produced when high-energy electrons, that are circulating around a storage ring at a constant energy, interact with a series of alternating magnets which causes deceleration radiation.

When X-rays interact with electrons, there are two types of scattering that occur: Compton scattering (inelastic scattering) and Thompson scattering (elastic scattering). Thompson scattering, where only the momentum is transferred, contains information on the electron distribution in a material. Constructive interference occurs when diffracted waves from elastic scattering interact with different atoms that are arranged in a periodic manner, such as in crystals. This produces sharp interference peaks[43]. The condition for a diffraction peak to occur can be written by Bragg's Law[44].

$$2d \sin \theta = n \lambda \quad (3-7)$$

where d is the inter-plane distance, θ is the scattering angle, n is an integer, and λ is the wavelength of the X-ray.

The two main types of XRD techniques are monochromatic powder XRD and energy-dispersive XRD. In this work, only powder XRD is utilized for characterization of samples. Different samples were studied by monochromatic angle-dispersive powder XRD measurements that were performed at the 12.2.2 beamline at the Advanced Light Source of Lawrence Berkeley National Laboratory at room temperature. A tunable Si(111) double-crystal in pseudo-channel-cut mode was used as a monochromator to filter “white” X-ray radiation and deliver X-rays of fixed but settable energies. The X-ray beam wavelength was $\lambda=0.4066 \text{ \AA}$. The X-ray beam was focused

to 30 x 30 μm using Kirkpatrick-Baez mirrors[45]. XRD patterns were collected with a MAR 345 Image Plate detector. Additionally, the monochromatic angle-dispersive powder X-ray diffraction (XRD) measurements at the 16BM-D beamline of the HP-CAT facility at the APS-ANL were performed. The X-ray wavelength of $\lambda=0.4066 \text{ \AA}$ was selected using a Si(111) double-crystal monochromator. XRD patterns were collected with a MAR 345 Image Plate detector. The instrumental parameters were calibrated using a CeO_2 standard. All diffraction images were integrated by Dioptas software[46] to produce intensity versus 2Θ patterns. Diffraction peaks were fit with background subtracted Voigt line profiles to obtain peak positions, intensities, and widths. UNITCELL[47] was used to refine the lattice parameters from all data. The pressure-volume data was fitted with the Birch-Murnaghan equation of state(EOS)[48] employing the EoSFit program[49].

E. X-ray absorption spectroscopy

Inner-shell spectroscopy utilizes interactions with deep-core electrons, and a commonly used form of this is X-ray absorption spectroscopy (XAS) which is used to investigate local electronic and geometric structure surrounding an atom. The basic physical process for XAS is depicted in Fig. 3-4. First, a deep-core electron with binding energy E_0 interacts with an incident X-ray. After this interaction, the electron is excited to a vacant state above the Fermi energy and a core-hole is left behind. A brief time later, two scenarios can occur: a higher state electron decays into the available core-hole and the remaining energy can (i) emit a photon or (ii) an Auger electron can be released [50].

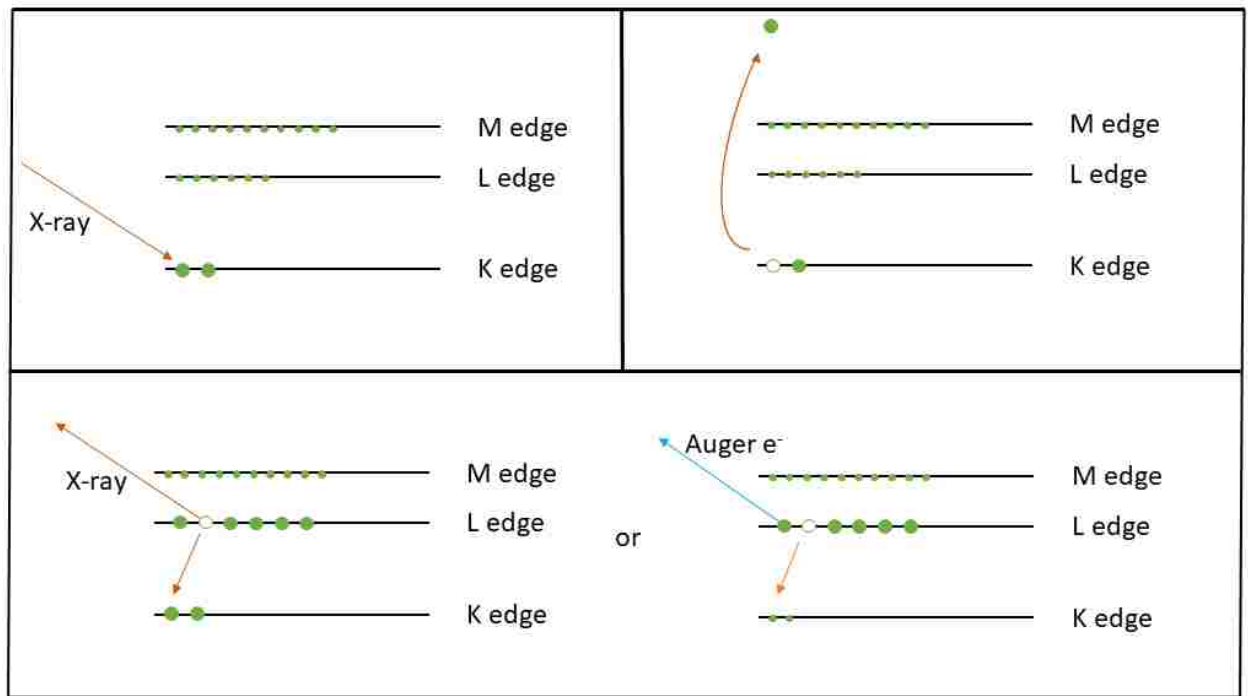


Figure 0-4 The basic physical process for X-ray absorption spectroscopy.

Each element has a specific pair of fluorescence and excitation energies which determines whether their K- or L-edges can be measured by hard or soft X-rays. For mercury ($Z=80$), the characteristic energies are defined in Table 3-2.

Edge	Energy (keV)	Line	Transition	Energy (eV)
K	83.109	L_I	$L_{III}M_I$	8722.6
L3	12.290	L_{α_2}	$L_{III}M_{IV}$	9898.1
L2	14.215	L_{α_1}	$L_{III}M_V$	9988.6
L1	14.835	L_{β_2}	$L_{III}N_V$	11926.3
		L_{β_1}	$L_{II}M_{IV}$	11822.7
		L_{γ_1}	$L_{II}N_{IV}$	13831.7

L_{β_4}	$L_{I}M_{II}$	11563.7
L_{β_3}	$L_{I}M_{III}$	11995.6
L_{γ_3}	$L_{I}N_{III}$	14267.2

Table 0-2 Characteristic excitation and fluorescence energies of Mercury[51].

For transmission XAS, Beer's Law for X-rays is defined as

$$\mu(E) = \ln \frac{I_0}{I_t}$$

where I_0 is the incident X-ray flux with energy E , I_t is the outgoing X-ray flux exiting from the sample, and $\mu(E)$ is the absorption coefficient which is dependent on the density of states with energy ($E-E_0$) at the absorbing atom.

A typical spectrum of an absorption edge can be divided into two separate regions: the X-ray absorption near-edge structure (XANES), which is the structure that is in the immediate area of the edge, and the extended X-ray absorption fine structure (EXAFS) which can extend from several hundred to one thousand eV beyond the edge [52]. Figure 3-5 depicts the XANES region with its various features. As the oxidation state of the sample increases under pressurization, the

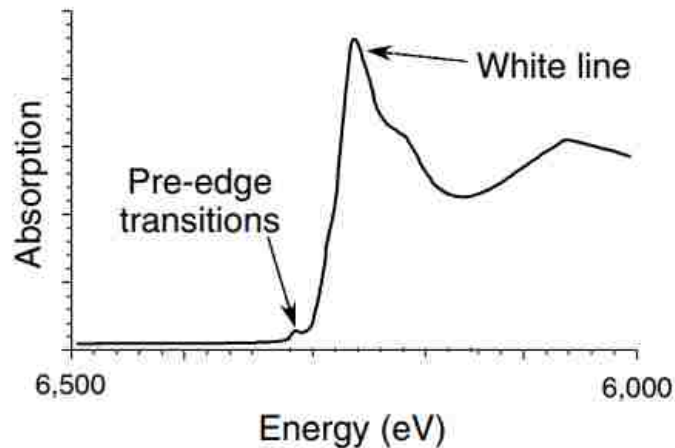


Figure 0-5 Various features in the XANES region (Redraw from [51]).

edge energy experiences a shift to higher energies. This is due to the higher charge of the atoms in an increased oxidation state which will require larger energy X-rays to remove the core electron.

F. Raman spectroscopy

When a transparent material has a beam of light passed through it, a small amount of energy from radiation is scattered. If radiation from a narrow band of frequency, or monochromatic radiation, the energy that is scattered will be comprised mainly of radiation of the incident frequency. This is known as Rayleigh scattering. However, there will be additional discrete frequencies above and below the incident frequency that are scattered. This component is known as Raman Scattering. [53]

Raman scattering can be as described. Photons and molecule collisions where energy is exchanged between the two (inelastic collisions) will result in the molecule gaining or losing energy based on quantum theory. Then the energy change will signify a vibrational/rotational energy change in the molecule. Radiation that is scattered at lower and higher frequencies is

denoted to as Stokes and anti-Stokes radiation respectively. At ambient conditions, most materials occur in their lowest vibrational states which means that Stokes radiation is more intense because anti-Stokes radiation requires a molecule to be in an excited vibrational state.

The Raman effect can be described by a molecule in a static electric field where the molecule becomes distorted and creates an electric dipole moment within the molecule. The separation of charges causes the molecule to be polarized. The magnitude of the deformation of the bond is defined by the polarizability constant, α . The induced dipole's size, μ , is dependent on the magnitude of the applied field, E , and α . When a beam of radiation with frequency ν , the induced dipole

$$\mu = \alpha E = \alpha E_0 \sin 2\pi\nu t$$

This can be expanded by a Taylor series and expanded with trigonometric relations to get

$$\mu = \alpha_0 E_0 \sin 2\pi\nu t + (0.5)\beta E_0 [\cos 2\pi(\nu - \nu_v)t - \cos\{2\pi(\nu + \nu_v)t\}]$$

Where β , α_0 , and ν_v represent the polarizability rate of change, the equilibrium polarizability, and the specific vibration of frequency. The anti-Stokes and Stokes in Raman scattering are represented through the terms with $(\nu \pm \nu_v)$. If the polarizability isn't altered by the vibration or rotation, then $\beta = 0$ and there is only oscillation at the incident radiation frequency. This means the molecular vibration/rotation is not Raman active.

Since Raman scattering has a dependence on the polarization of a bond, fluorescence becomes problematic when the energy of the photon is not enough to excite the electronic transitions within a material. In these cases, it is necessary to utilize other methods like infrared spectroscopy due to the dipole moment shaping the interactions between the radiation and the molecule.

Raman spectra of the samples in this thesis were confined and compressed in a DAC at room temperature were measured using an ISA HR460s spectrometer with a Peltier-cooled CCD detector (Andors 1024 128 pixels). The resolution of the spectrometer was approximately $\approx 1 \text{ cm}^{-1}$. The excitation source was a Coherent® diode-pumped multiline laser tuned to 532 nm.

CHAPTER 4: STRUCTURAL PROPERTIES OF HgF₂ AT HIGH PRESSURE

Mercury difluoride (HgF₂) is widely used in synthetic organic chemistry as a selective fluorination agent [54] and as a mediating agent [55]. Additionally, theoretical studies of (HgF₂)_n clusters demonstrated that HgF₂ in an extended solid exhibits remarkable chemical bonding properties [56]. Moreover, it has been predicted that at extreme conditions, when Hg interacts with strong oxidizing agents, such as fluorine [2,6] the Hg-based compounds where mercury has unusual oxidation states (+3 or +4) can be synthesized [29,57,58]. Under ambient conditions, HgF₂ exhibits the cubic CaF₂ structure with the space group *Fm-3m* [59]. Thus far, only one attempt has been made to investigate the high pressure structural properties of HgF₂, but due to the compound's high moisture reactivity it was unsuccessful [60]. Nevertheless, the high-pressure study of HgF₂ was performed from the theoretical point of view [61] and only one cubic to orthorhombic (*Pnma* space group) phase transition at 4.7 GPa has been predicted. In this chapter an experimental investigation of high pressure induced structural behavior of HgF₂ is presented which provides more insights into the structural properties of mercury-fluorine compounds at high pressure.

A. Purification of HgF₂ by high pressure ramp process

Samples of powdered HgF₂ were loaded into a DAC and sealed under an inert argon atmosphere to prevent sample hydration and were then investigated by means of synchrotron XRD at BL12.2.2 at the ALS as described in more detail in Chapter III. Fig. 4-1a shows the initial XRD pattern of ambient HgF₂ compared to the previously reported cubic crystal structure [59] with space group *Fm-3m*. The initial structure is comprised of the five cubic crystal structure peaks

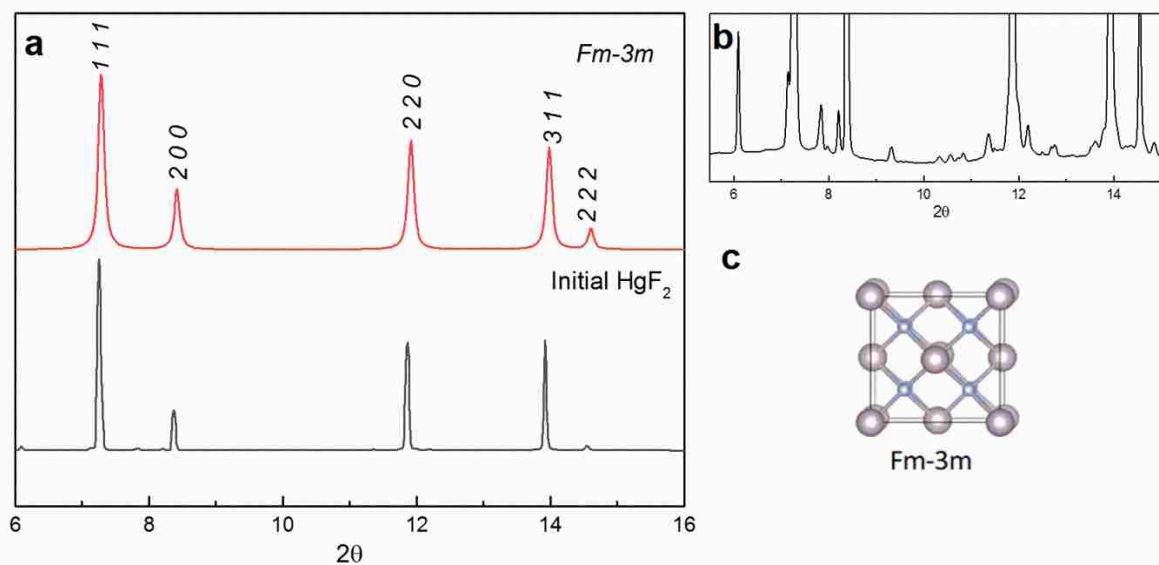


Figure 0-3 XRD patterns of (a) the initial HgF_2 sample at ambient conditions, (b) the combined sample of HgF_2 and XeF_2 at 12 GPa, and (c) the purified HgF_2 sample at ambient conditions. Vertical dark red bars represent the tetragonal crystal structure of xenon difluoride[59] with Fm-3m space group.

along with numerous peaks which correspond to impurities (see Fig. 4-1b) as the initial material was only 97% pure (see Chapter III).

One of the main focuses of our research group is to experimentally investigate unusual oxidation states in Hg-based compounds at high pressure. Previous theoretical predictions suggested that HgF_2 pressurized above 50 GPa in the presence of F_2 molecules will possibly transform into HgF_4 . Thus, in our attempts to verify these predictions we have considered the mixture of HgF_2 and XeF_2 as viable system, as XeF_2 can be considered as a potential source of fluorine[62,63], and thus a necessary component for HgF_4 synthesis at high pressure. In our studies we observed, that a high pressure ramp (HPR)[64] process applied to the mixture of HgF_2 and XeF_2 loaded in a DAC can be considered as a possible route for HgF_2 purification. Indeed, the large presence of impurities observed in the initial HgF_2 samples (see Fig. 4-1b) may significantly contribute to the structural

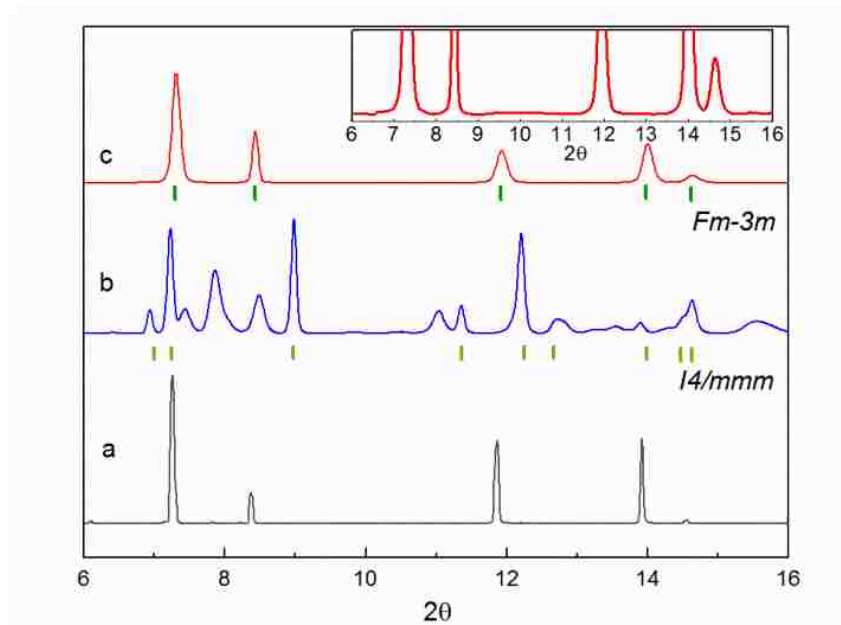


Figure 0-4 XRD patterns of HgF₂ and XeF₂ at 12 GPa, and (c) the purified HgF₂ sample at ambient conditions. Vertical dark red bars represent the tetragonal crystal structure of xenon difluoride[65] with the *I4/mmm* space group and the vertical green bars correspond to the cubic crystal structure of mercury difluoride[59] with *Fm-3m* space group.

behavior of the studied material at high pressure. We note that a previous attempt to study HgF₂ under high pressure was not successful due to a high moisture contamination[60]. Fig. 4-2 displays the initial XRD pattern of HgF₂ which is also presented in previous Fig. 4-1b compared to the sample of mixed HgF₂ and XeF₂ pressurized at 12 GPa and the final HgF₂ product obtained after purification. Vertical dark red and green bars represent the tetragonal crystal structure of xenon difluoride[65] at 11 GPa with the *I4/mmm* space group and the cubic crystal structure of mercury difluoride[59] with *Fm-3m* space group, correspondingly. The HgF₂ purification process consisted of following steps: (i) compression of the HgF₂ and XeF₂ mixture above 10 GPa, and (ii) decompression to 0 GPa. After the decompression step, XeF₂ decomposes to a gas due to the low vapor pressure (6.0×10^2 Pa at 298 K) at ambient temperatures[66] and escapes from the gasket. We hypothesize that during this process, impurities trapped within HgF₂ react with molecular

fluorine released during the XeF_2 decomposition and due to its high electronegativity form XF_n (X represents impurities) compounds which escape from the sample chamber. The final product from purification results in an XRD pattern of the expected cubic crystal structure ($Fm-3m$) that lacks any additional peaks (see insert in Fig. 4-2). We should note that a more complete understanding of the HgF_2 purification mechanism requires more detailed investigation which will be addressed in our future research project.

B. HgF_2 at high pressures

After purification, we investigated the structural properties of the purified HgF_2 under pressure. Fig. 4-3a shows XRD patterns at selected pressure points up to 2.5 GPa. Above this pressure, the complete structural transformation of the initial cubic structure is observed (see Fig. 4-5a). Thus, to investigate the high pressure behavior of the initial cubic structure only, we first considered only the 0-2.5 GPa pressure range. The first XRD pattern depicted in Fig. 4-3a is the XRD pattern obtained at ambient pressure. It matches the previously reported cubic crystal structure of HgF_2 with $Fm-3m$ space group[59]. Upon pressurization, (up to 1.72 GPa) no changes in the XRD patterns are observed which indicates that HgF_2 does not undergo any structural transformations in this pressure range. However, the formation of new peaks appears when the sample is pressurized to 2.5 GPa. A new small peak emerges at 6.2° and two peaks at 7.8° and 8.3° also form. Additionally, as depicted in Fig. 4-3a the XRD pattern of HgF_2 pressurized to 2.5 GPa exhibits one small peak at 10.7° , and several new peaks in the 15.2° to 19.1° 2θ range (the total characterization of novel crystal structure is discussed below). Despite this, all seven peaks from the original structure are present in the XRD pattern at 2.5 GPa.

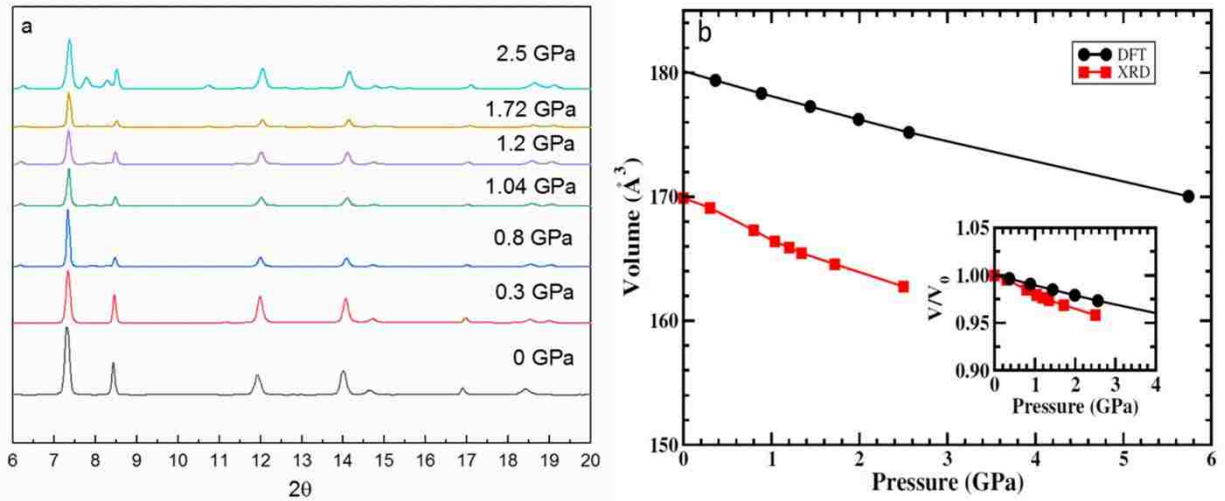


Figure 0-5 (a) XRD patterns of HgF₂ at selected pressure points up to 2.5 GPa. (b) The unit cell volume as a function of pressure for HgF₂ in the space group *Fm-3m* phase as determined experimentally (red curve) and theoretically (black curve), the inset plot represents the normalized change of volume vs. pressure.

The structural parameters of the cubic (*Fm-3m*) phase were extracted from the diffractions patterns and first principle calculations. The corresponding volume changes are plotted *versus* pressure increase in Fig. 4-3b. The lattice parameters of the cubic (*Fm-3m*) phase were extracted from the diffractions patterns and fit using a cubic unit cell up to 1.7 GPa (Table 4-1).

Table 0-1 Observed and calculated *d* spacings for the fluorite-type phase of HgF₂ at 0 GPa. These peaks are fit to an cubic unit cell with $a = 5.5327 \text{ \AA}$ and $V=169.367 \text{ \AA}^3$.

<i>h</i>	<i>k</i>	<i>l</i>	d_{obs} (\AA)	d_{calc} (\AA)	Δd (\AA)	Intensity (%)
1	1	1	3.19068	3.1976	0.00692	100
2	0	0	2.76578	2.7700	0.00422	47
2	2	0	1.95646	1.9590	0.00254	28
3	1	1	1.66773	1.6703	0.00257	33
2	2	2	1.59646	1.5993	0.00284	6
4	0	0	1.38256	1.3850	0.00244	9
3	3	1	1.27043	1.2709	0.00047	7

The corresponding volume changes are plotted *versus* pressure increase in the inset in Fig. 3b. The volume-pressure dependence up to 1.7 GPa was described using a third-order Birch-Murnaghan equation of state, and the results are presented in Table 1. The fit to the experimental data (red curve in Fig. 4-6b) between 0 and 1.7 GPa resulted in a fit bulk modulus of $K_0 = 94.4$ GPa and a zero-pressure volume of $V_0 = 168.6 \text{ \AA}^3$ when the pressure derivative of the bulk modulus, K_0' , was fixed at 4.7 which is similar to previously reported theoretical studies of HgF_2 [67,68]. We note that in the previous theoretical study, the high pressure induced phase transition of HgF_2 from the $Fm-3m$ cubic structure to the $Pnma$ orthorhombic crystal structure was suggested at 4.7 GPa[61].

Table 0-2 Equation of state parameters for HgF_2 . Asterisk (*) represents fixed values.

Reference	V_0 (\AA^3)	K_0 (GPa)	K_0'
<u>Fluorite-type</u>			
This work ^a	168.6	94.4	4.7*
This work ^b	180.1	86.9	4.7*
Theory[68]	163.67	117.03	-
Theory[67]	163.04-179.69	88.5-133.3	-
<u>Cotunnite-type</u>			
This work ^a	156.4	92.9	4.7*
This work ^b	166.9	72.5	4.7*

^a X-ray diffraction experiment

^b Theoretical calculation

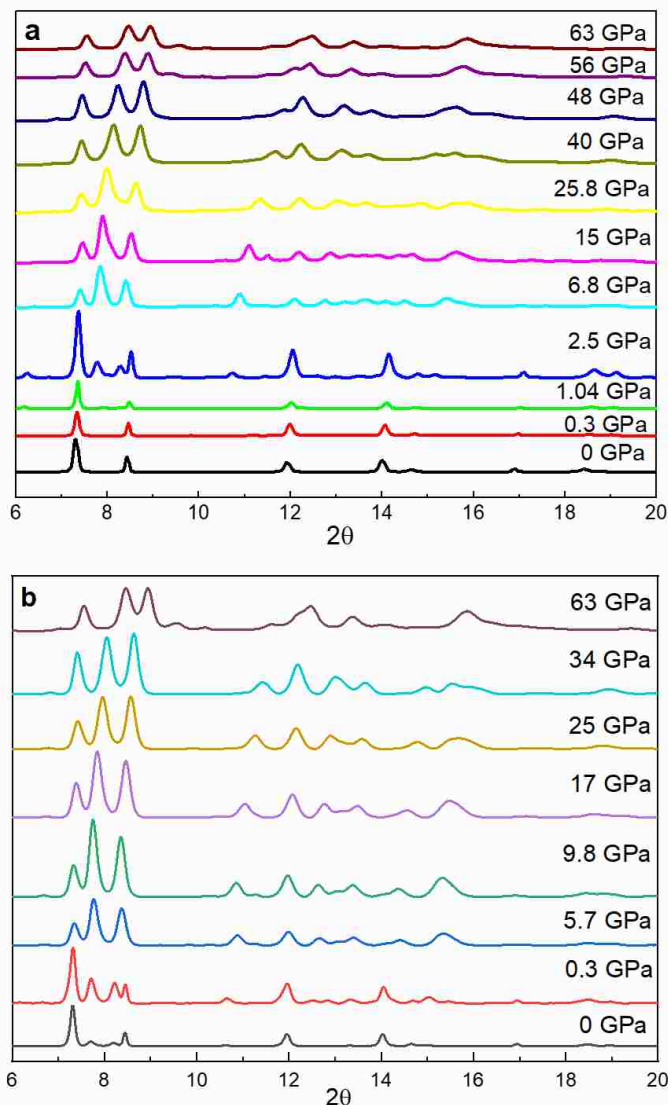


Figure 0-6 XRD patterns of HgF₂ at selected pressure points (a) upon compression to 63 GPa and (b) upon decompression.

Finally, we examined the structural properties of HgF₂ pressurized up to 63 GPa. Fig. 4-6a, shows the XRD patterns of HgF₂ at selected pressure points in the 0-63 GPa pressure range. Powdered HgF₂ pressurized above 2.5 GPa undergoes a structural transformation with the formation of a new crystal structure (6.8 GPa in Fig. 4-6a). Further pressurization up to 63 GPa does not significantly change the XRD patterns of new HgF₂ phase with the exceptions that the intensity of most peaks from the original structure decrease and that the diffraction peaks shift

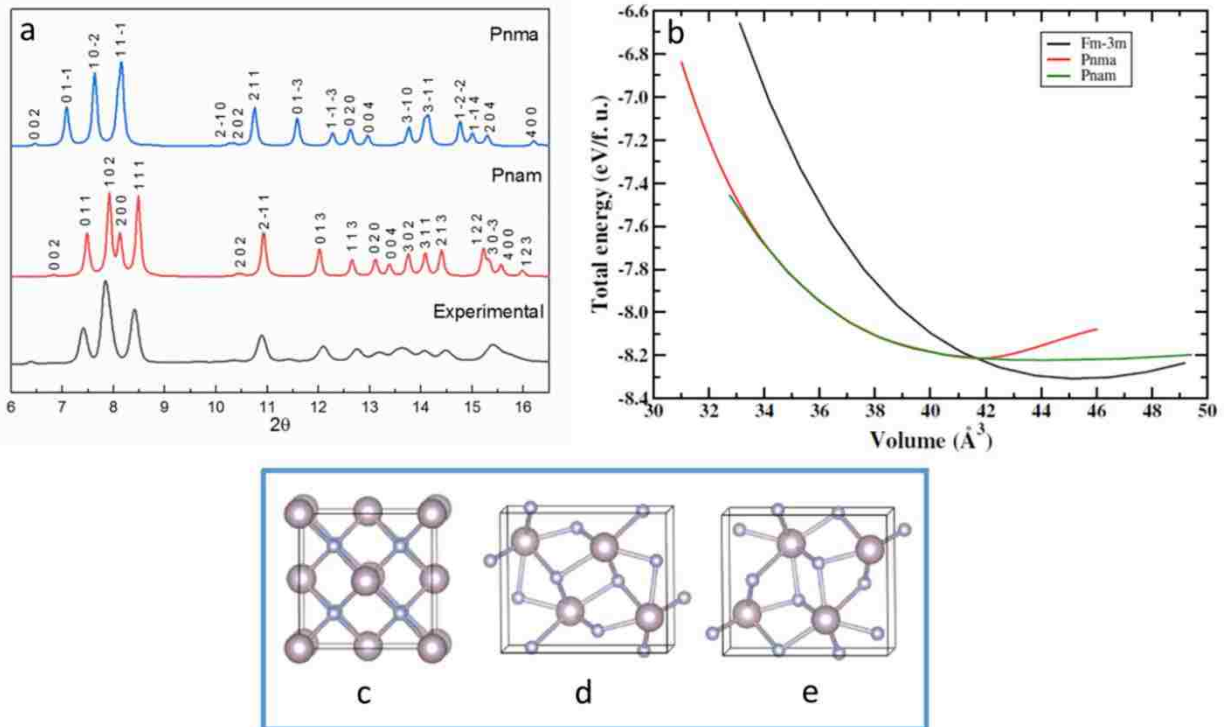


Figure 0-7 (a) XRD patterns of the experimentally obtained at 6.8 GPa and theoretically predicted orthorhombic crystal structures with the space groups *Pnam* and *Pnma* where diffraction peaks are labeled with Miller indices; (b) the calculated total energy curves of the corresponding phases; Ball and stick models of crystal structures of HgF_2 : (c) the cubic *Fm-3m* structure in the ambient conditions, (d) the *Pnam* space group with the lattice parameters $a=5.96 \text{ \AA}$, $b=3.64 \text{ \AA}$, and $c=7.14 \text{ \AA}$ at 6.1 GPa, and (e) the *Pnma* space group with the lattice parameters $a=5.77 \text{ \AA}$, $b=3.70 \text{ \AA}$, and $c=7.21 \text{ \AA}$ at 6.38 GPa. Grey and yellow spheres represent Hg and F atoms respectively.

toward higher angle with increasing pressure which indicates that the lattice planes distances decrease upon compression. Decompression from 63 GPa to ambient pressure (Fig. 4-5b) results in the coexistence of two phase states. Among the XRD peaks which correspond to the initial *Fm-3m* cubic crystal structure additional small peaks are observed (0 GPa in Fig. 4-5b) which is due to the structural hysteresis of HgF_2 .

The lattice parameters and volume of HgF_2 from 2.8 to 63 GPa were fit using an orthorhombic unit cell and presented in Table 4-3. The variation in measured experimental lattice parameters as a function of pressure are shown in Fig. 5b. A fit to our data in the orthorhombic

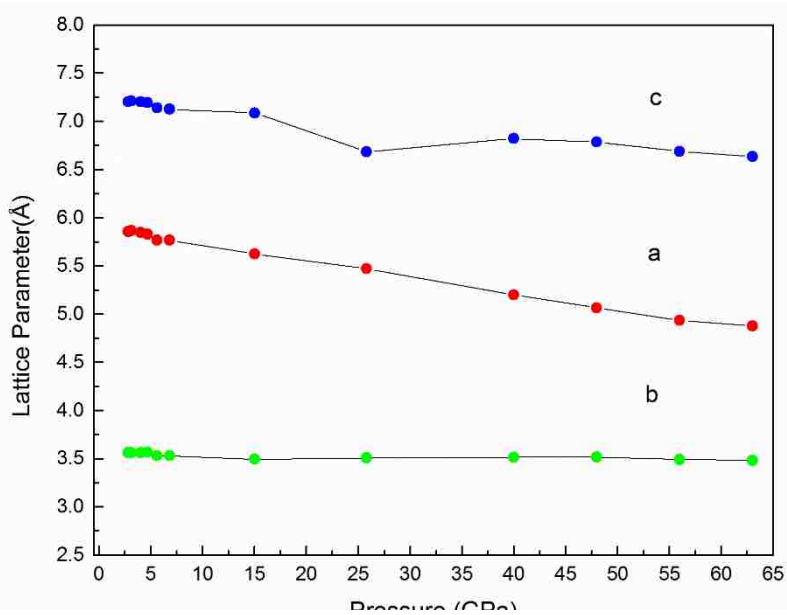


Figure 0-8 Lattice parameters of the cotunnite-type phase of HgF₂.

phase resulted in a zero-volume pressure $V_0=156.4 \text{ \AA}^3$ and a bulk modulus of $K_0=92.9 \text{ GPa}$ when the pressure derivative of the bulk modulus was held fixed at 4.7. Compared to our theoretical calculation of $K_0= 72.5 \text{ GPa}$ which are both less than our original bulk modulus in the fluorite phase. The lattice parameters decrease linearly with a decreasing the fastest as shown in Figure 4-11.

Table 0-3 Observed and calculated d spacings for the cotunnite-type phase of HgF₂ at 5.6 GPa. The peaks are fit to a orthorhombic unit cell with $a = 5.7678 \text{ \AA}$, $b = 3.5334 \text{ \AA}$, $c = 7.1388 \text{ \AA}$, and $V= 145.490 \text{ \AA}^3$.

h	k	l	d_{obs} (\AA)	d_{calc} (\AA)	Δd (\AA)	Intensity (%)
0	0	2	3.64779	3.56941	0.07837	2
0	1	1	3.15199	3.16675	-0.01476	39
1	0	2	2.97937	3.03522	-0.05585	100
1	1	1	2.77589	2.77589	-0.00085	67
2	1	1	2.14269	2.13223	0.01046	29

Complementary first-principles calculations have been carried out in this study to identify a new crystal structure formed above 2.5 GPa (see Fig. 4-4a). The density functional theory (DFT)

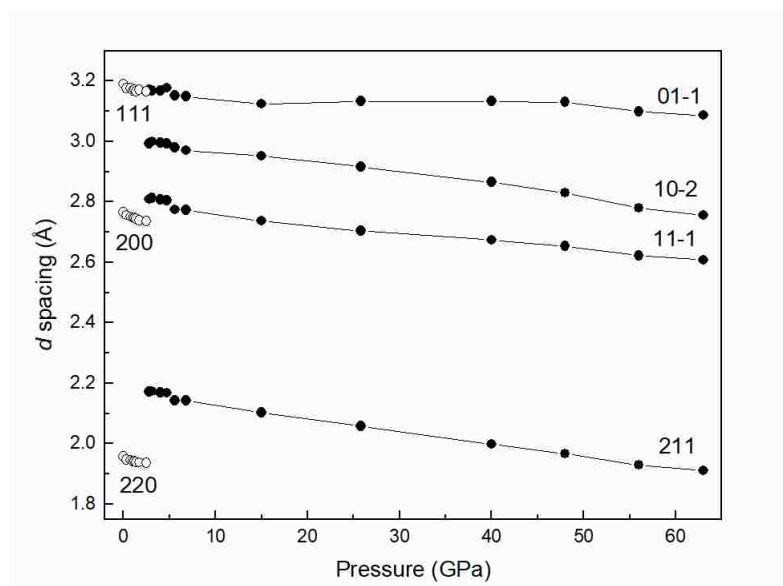


Figure 0-9 Interplanar spacing difference over the studied pressure range (fluorite-type to cotunnite-type phases) for HgF₂.

analysis suggested two candidate orthorhombic crystal structures with space groups *Pnma* and *Pnam* which are depicted in Fig. 4-5a. The optimized atomic positions and lattice constants are summarized in Table 4-4.

Table 0-4 Predicted lattice parameters and atomic positions of two candidate orthorhombic HgF₂ phases at around 6 GPa. The *Pnam* phase is the orthorhombic cotunnite-type PbCl₂ structure.

		Lattice Parameters (Å)			Atomic Positions		
		a	b	c	Hg (4c)	F1 (4c)	F2 (4c)
Pnam	Theory	5.960	3.645	7.137	0.2578,	0.8566,	0.4777,
	Z=4; P=6.1 GPa				0.25,	0.25,	0.25,
					0.1131	0.0748	0.8305
Pnma	Theory	5.771	3.699	7.205	0.7596,	0.3534,	0.0223,
	Z=4; P=6.39 GPa				0.25,	0.25,	0.75,
	X-ray diffraction P=6.8 GPa	5.767	3.532	7.125	0.1107	0.0762	0.3305

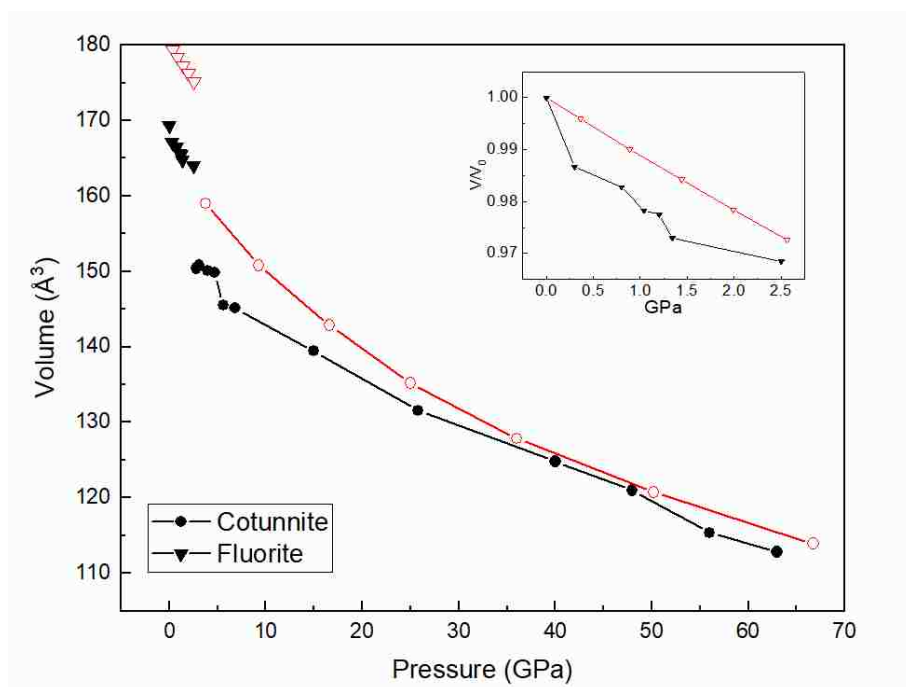


Figure 0-10 Pressure vs. volume data over the whole pressure range for the experimental (black curve) and the theoretical (red curve) data.

Additionally, Fig. 4-7d and 4-7e display the 3D structures of the theoretically predicted candidate crystal structures of HgF_2 . Although, these candidate structures do not completely correspond to the experimentally obtained HgF_2 XRD pattern, they suggest that a new high pressure phase of HgF_2 (above 2.5 GPa) exhibits structural properties of both proposed $Pnma$ and $Pnam$ structures, respectively.

The calculated total energy curves indicated, as shown in Fig. 4-5e, that the pressure induced phase transitions from the low pressure $Fm-3m$ phase (black line) to the high pressure orthorhombic phases, either to $Pnma$ (red line) at 4.9 GPa or to $Pnam$ (green line) at 4.7 GPa may occur. It is also found that both $Pnma$ and $Pnam$ phases are energetically compatible in the pressure ranges that the transition occurs with the energy difference of less than 6 meV.

In summary, we provided an experimental investigation of the high pressure induced structural behavior of HgF_2 up to 63 GPa. We demonstrated that by applying the high pressure

ramp technique, to the mixture of powdered HgF_2 and crystalline XeF_2 , the initial HgF_2 can be purified. The pure HgF_2 exhibits the previously reported cubic structure with $Fm-3m$ space group, and the structural properties of this structure were investigated up to 2.5 GPa. Above 2.5 GPa, a phase transition from cubic to orthorhombic structure was found and by first principle calculations two candidate structures with $Pnma$ and $Pnam$ space groups were proposed. Our experiments demonstrated that the high pressure HgF_2 orthorhombic structure is stable up to 63 GPa and reversible (with slight structural hysteresis) to the initial cubic structure upon decompression.

CHAPTER 5: INVESTIGATION OF HgF₄ AT HIGH PRESSURE

In chapter 2, we presented a brief description about previous theoretical and experimental investigations of HgF₄ synthesis at various conditions. Nevertheless, thermodynamically stable HgF₄ has not been experimentally observed. Herein, we discuss the investigation of the high pressure induced synthesis of HgF₄.

Our effort for X-ray induced synthesis of HgF₄ was performed at the High Pressure Collaborative Access Team's (HP-CAT's) 16 BM-B beamline at the Advanced Photon Source using "white" polychromatic X-rays. A symmetric-style DAC was used for pressurization purposes (see chapter 3). For investigation of HgF₄ synthesis, several samples of HgF₂ and XeF₂ mixture were irradiated with the white beam for more than five hours each at pressures above 10 GPa to avoid any material losses triggered by the X-ray induced decomposition of XeF₂ (via $\text{XeF}_2 + h\nu \rightarrow \text{Xe} + \text{F}_2$). We note that all samples of XeF₂ escaped the sample chamber after X-ray irradiation if initially pressurized below 10 GPa due to the pressure drop in DAC. X-ray irradiated and un-irradiated samples were characterized by means XRD, Far-IR, XAS spectroscopy pressurized up to 50 GPa for comparison purposes. Fig. 5-1 displays an example of the sample before and after X-ray irradiation at different pressure point.

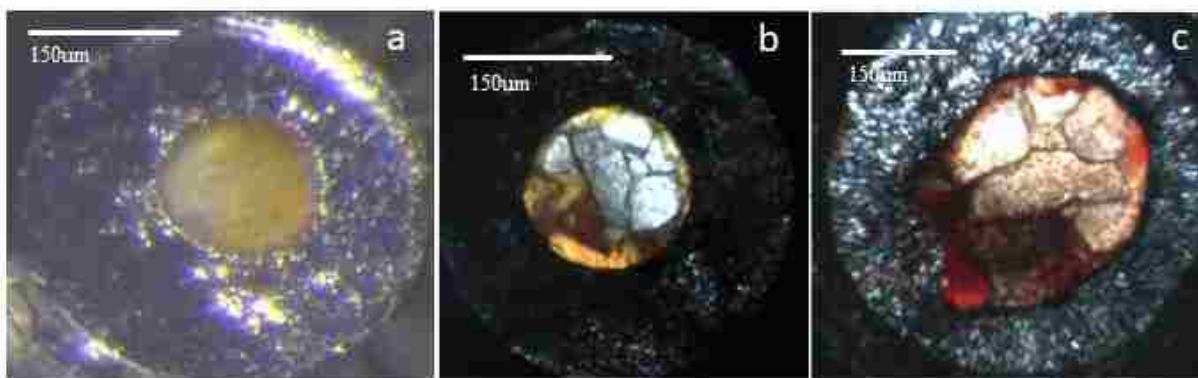


Figure 0-1 Pictures of HgF₂ and XeF₂ mixture at high pressure; pressurized (a) above 10 GPa before X-ray irradiation, (b) above 20 GPa after X-ray irradiation, and (c) the same sample at 53 GPa.

A. XRD characterization of irradiated HgF₂ XeF₂ samples

Fig. 5-2 shows a X-ray produced 2-D map of the sample including the irradiated regions within the sample. Four different regions within the sample were probed by XRD when the sample was pressurized at different pressures. Namely, the dark area, bright area middle, bright area edge and average area regions.

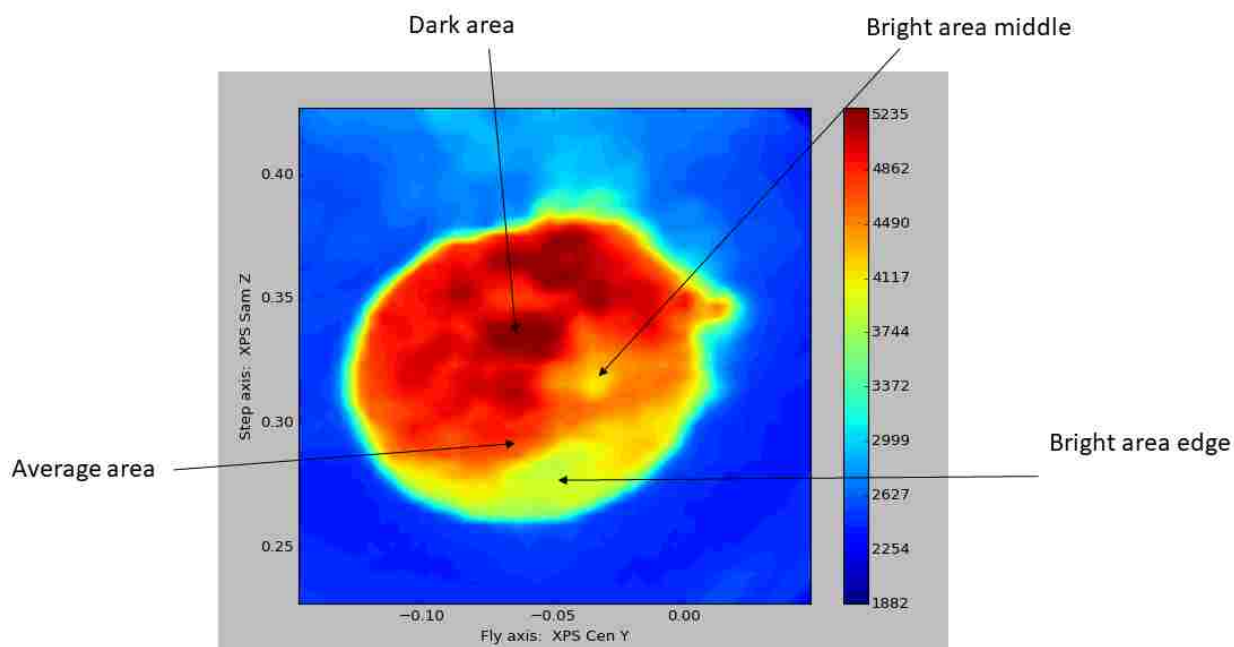


Figure 0-2 X-ray produced 2-D map of irradiated HgF₂ XeF₂ sample, XRD probed areas are named according to the brightness of obtained image color.

First, we present the XRD study of the “average area” in the irradiated HgF₂ XeF₂ sample. Fig. 5-3 depicts *in situ* XRD patterns obtained at different pressure points as well as XRD patterns of the initial HgF₂ cubic crystal structure with the *Fm-3m* space group and the XeF₂ tetragonal structure with the *I4/mmm* space group at 8.5 GPa correspondingly. The XRD pattern obtained at 7.6 GPa clearly demonstrates that “average area” in the X-ray irradiated sample contains XeF₂ and

a high pressure phase of HgF₂ (orthorhombic structures with the space groups *Pnam* and *Pnma* see Figure 4-10) and no initial HgF₂ cubic structure is observed.

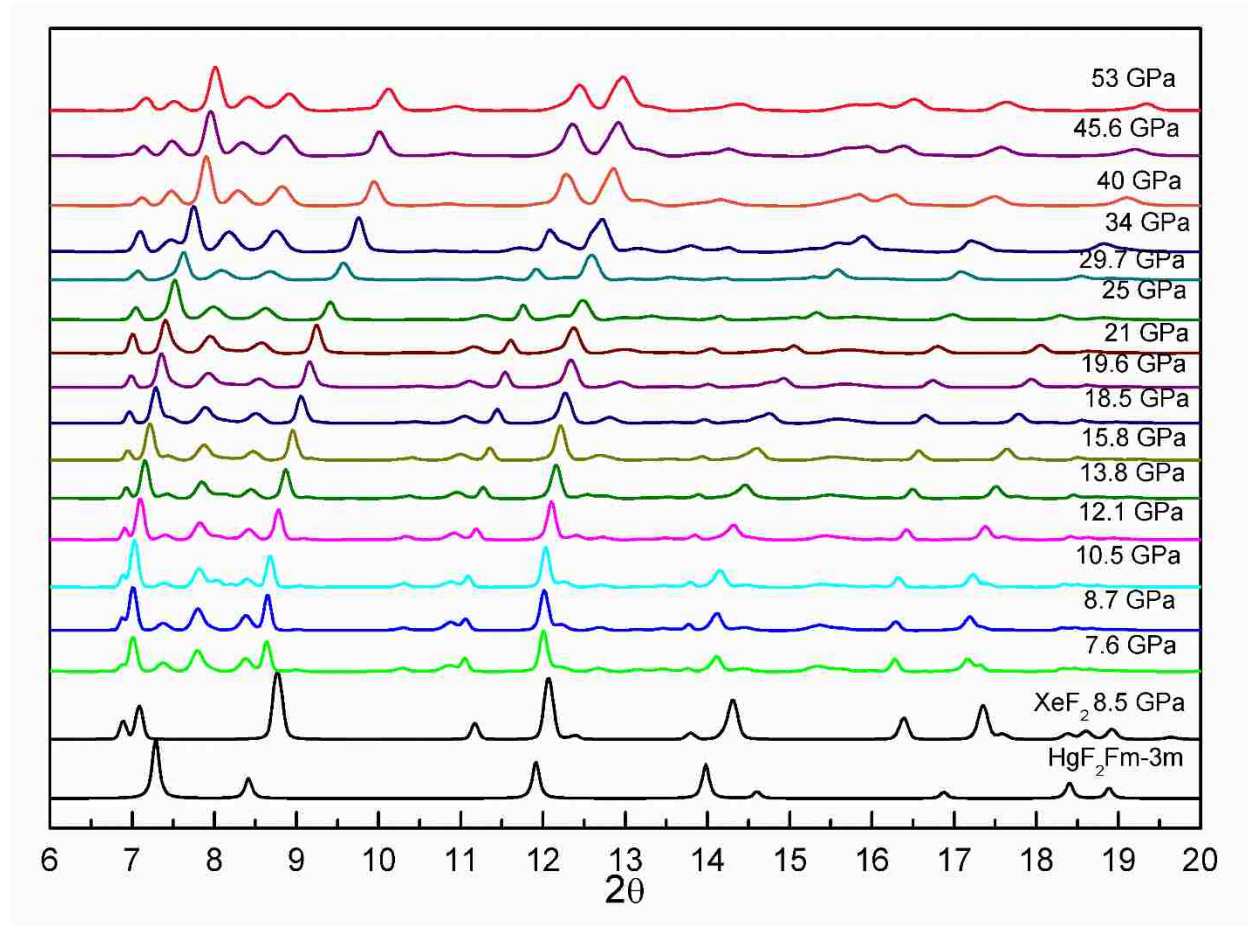


Figure 0-3 XRD patterns of: “average area” in the irradiated HgF₂ XeF₂ sample, initial HgF₂ cubic structure with space group *Fm-3m* and of XeF₂ tetragonal structure with *I4/mmm* space group at 8.5 GPa.

Further pressurization up to 53 GPa does not induce any major XRD pattern changes with the exceptions that the intensity of most peaks from the system’s structure obtained at 7.6 GPa decrease and that the diffraction peaks shift toward higher angle with an increasing pressure. This indicates that the lattice planes distances decrease upon compression.

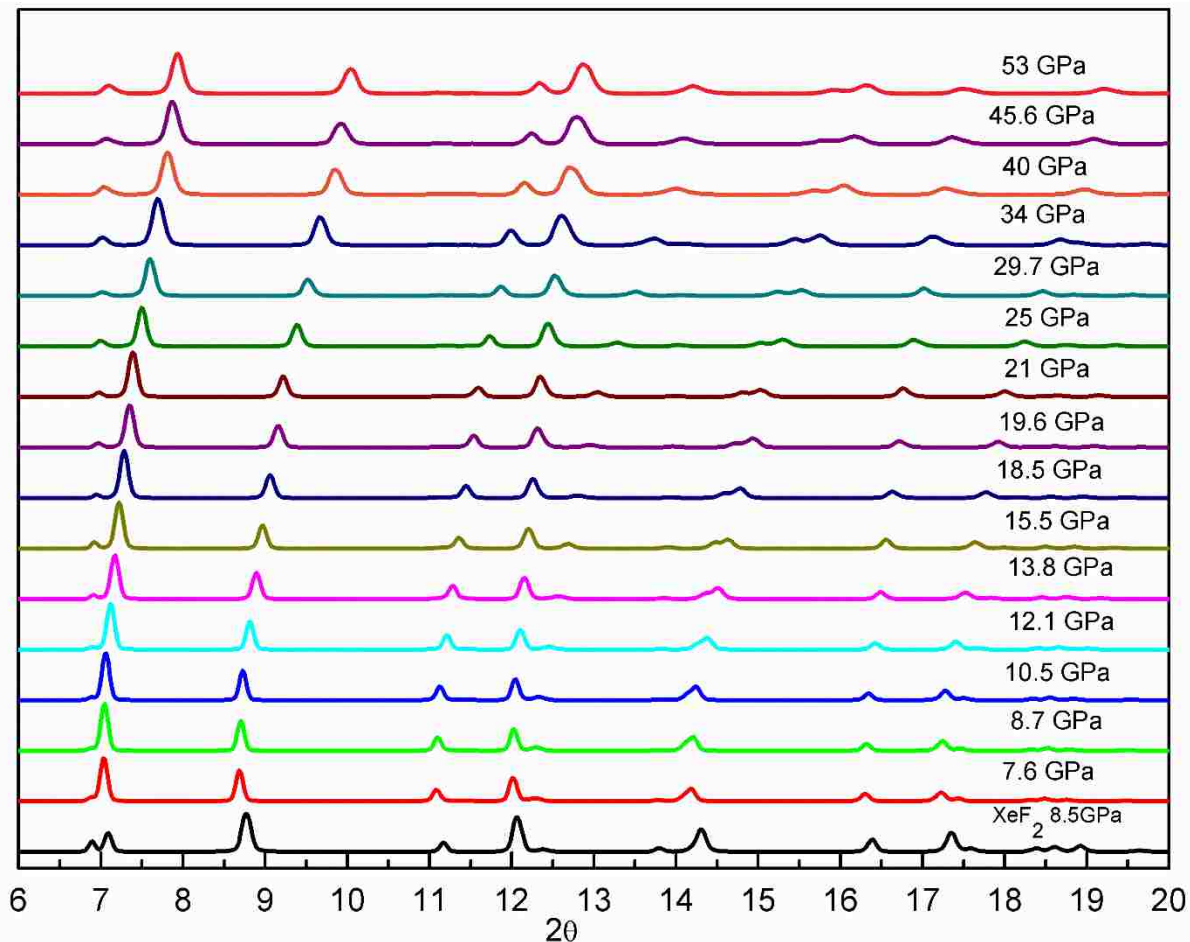


Figure 0-4 XRD patterns of: “dark area” in the irradiated HgF_2 XeF_2 sample and of XeF_2 tetragonal structure with $I4/mmm$ space group at 8.5 GPa.

The next area of the irradiated HgF_2 and XeF_2 sample examined by XRD was the “dark area” (see Fig. 5-2). Fig. 5-4 presents the XRD patterns of the “dark area” at different pressures and the XeF_2 tetragonal structure with the $I4/mmm$ space group at 8.5 GPa. As it can be seen from the figure the “dark area” contains only XeF_2 compound which upon pressurization behaves in a good agreement with previously reported studies of XeF_2 high pressure behavior[65]. In their study it has been demonstrated that the $I4/mmm$ XeF_2 structure undergoes phase transition to $Immm$ structure at 31 GPa which is also observed in our studies around 29 GPa (see Fig. 5-4).

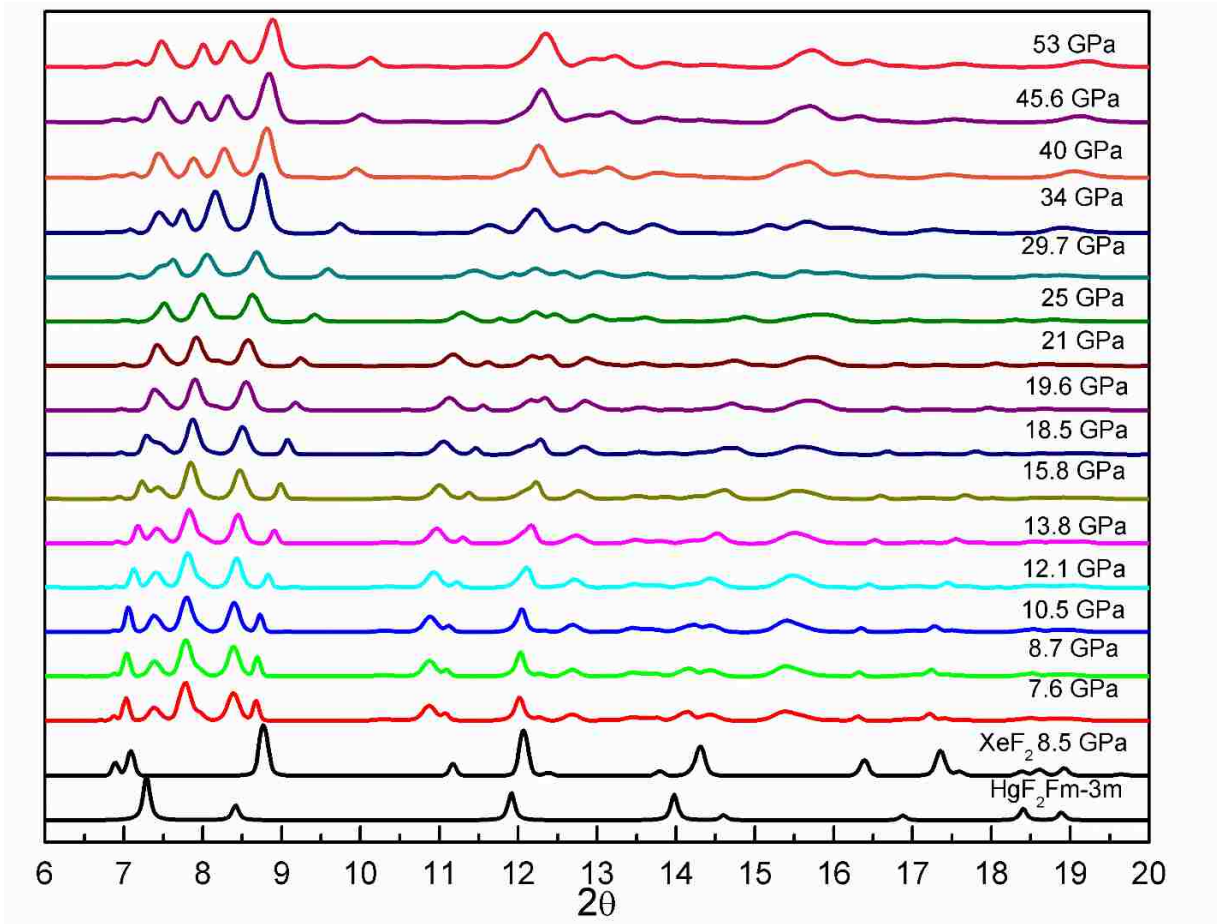


Figure 0-5 XRD patterns of: “bright area middle” in the irradiated HgF_2 XeF_2 sample, initial HgF_2 cubic structure with space group $Fm-3m$ and of XeF_2 tetragonal structure with $I4/mmm$ space group at 8.5 GPa.

The third area in the irradiated HgF_2 and XeF_2 sample which was investigated by means of XRD was the “bright area middle” (see Fig. 5-2). Fig. 5-5 displays the XRD patterns obtained at different pressure points and XRD patterns of the initial HgF_2 $Fm-3m$ cubic crystal structure and the XeF_2 $I4/mmm$ tetragonal structure obtained at 8.5 GPa. The XRD pattern obtained at 7.6 GPa shows that the “bright area middle” in the X-ray irradiated sample contains slight amounts of XeF_2 but most of the observed peaks represent the high pressure phase of HgF_2 (orthorhombic structures with the space groups $Pnam$ and $Pnma$ see Figure 4-10). Pressurization up to 53 GPa is similar to the “average area” case. No significant XRD pattern changes are observed upon the pressure

increase. Only peaks broadening indicating the decrease in the scale of crystal grains and shifts of peaks toward high angle which represents that all lattice plane become closer are detected.

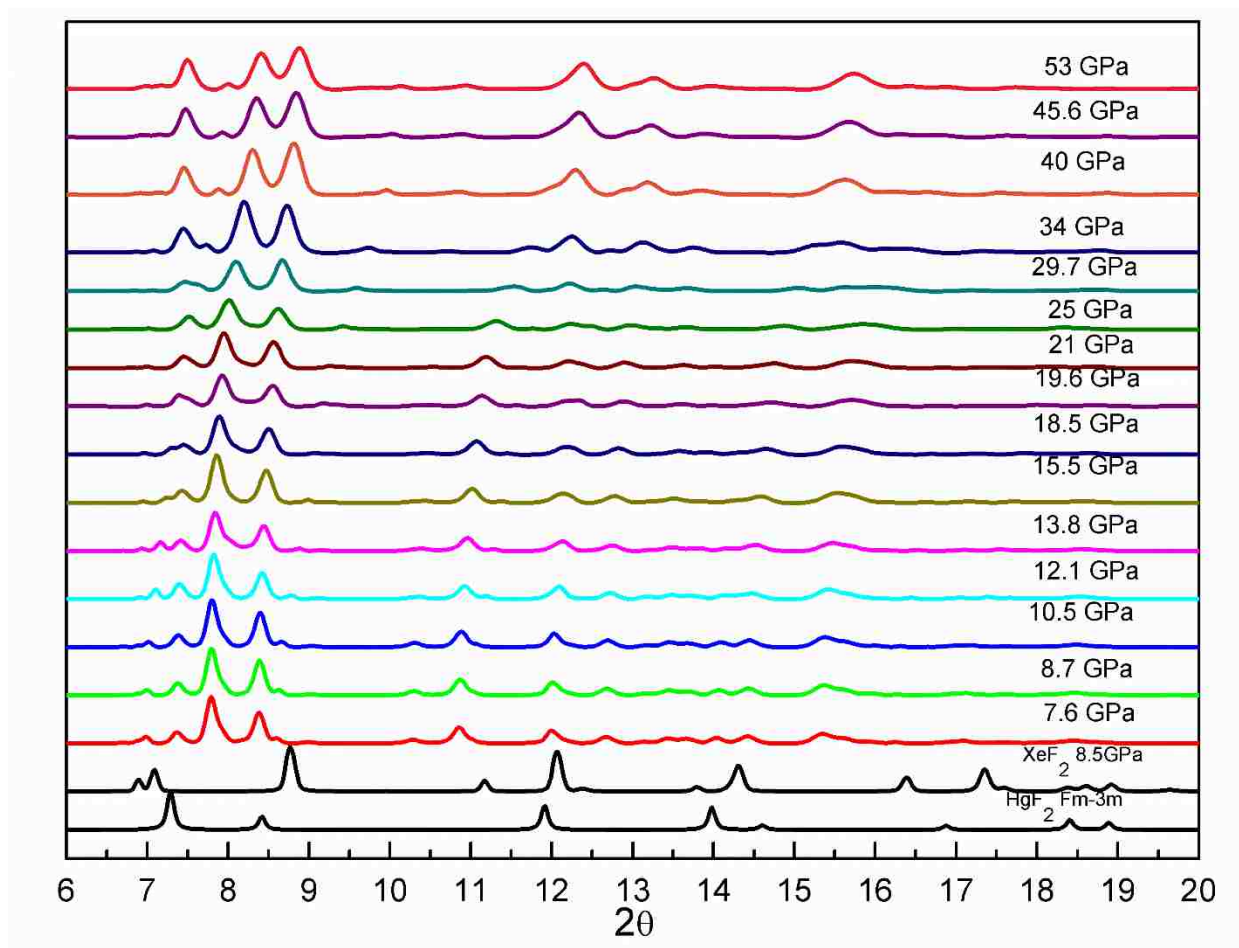


Figure 0-6 XRD patterns of: “bright area edge” in the irradiated HgF₂ XeF₂ sample, initial HgF₂ cubic structure with space group *Fm-3m* and of XeF₂ tetragonal structure with *I4/mmm* space group at 8.5 GPa.

The picture dramatically changes in the case of “bright area edge” in the irradiated HgF₂ XeF₂ sample as shown in Fig. 5-6. The XRD pattern obtained at 7.6 GPa is the high pressure phase of HgF₂ only and no peaks from XeF₂ is presented. Based on previous case where only the slight presence of XeF₂ was found and the “bright area edge” case we can conclude that the brightest

area in the irradiated HgF_2 XeF_2 contains the smallest amount of XeF_2 (see Fig. 5-2). The high pressure behavior of this area corresponds to HgF_2 case considered in Chapter 4.

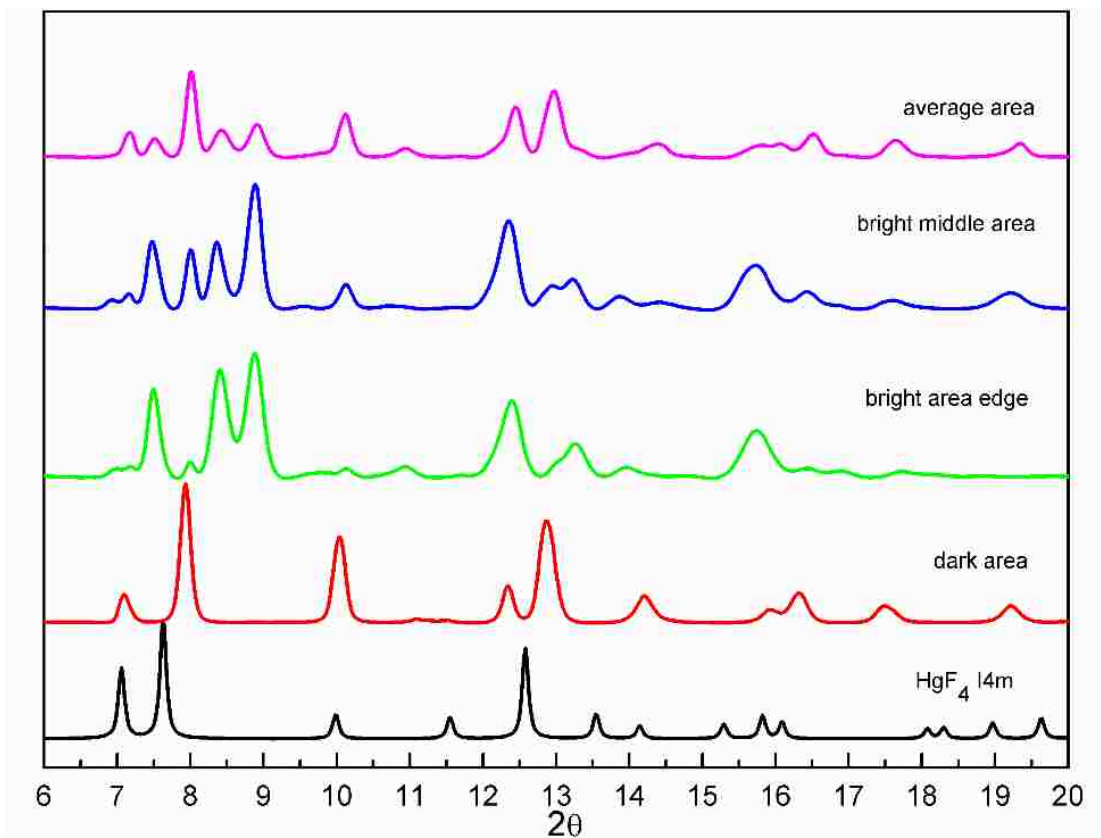


Figure 0-7 XRD patterns comparison of different areas in the irradiated HgF_2 XeF_2 sample obtained at 50 GPa and predicted tetragonal structure of HgF_4 with the $I4/m$ space group [6].

Finally, we compared the XRD patterns of different areas in the irradiated HgF_2 and XeF_2 sample obtained at 50 GPa (see Fig. 5-7) with the predicted $I4/m$ tetragonal structure of HgF_4 . As it can be seen from the figure, none of the XRD patterns contain peaks belonging to the HgF_4 structure, indicating that a pressure of 53 GPa is not enough for the efficient synthesis of the thermodynamically stable HgF_4 which formation was previously theoretically predicted at this

pressure[6]. Nevertheless, we can suggest that the formation of HgF_4 should be expected at higher pressure as, for instance, it was predicted for HgF_3 (73 GPa).

B. XRD characterization of unirradiated HgF_2 XeF_2 samples

Fig. 5-8 shows a X-ray produced 2-D map of the sample with the studied regions from it. There are 2 different regions within the sample which were probed by XRD when the sample was pressurized at different pressure. Namely, dark area, and middle area.

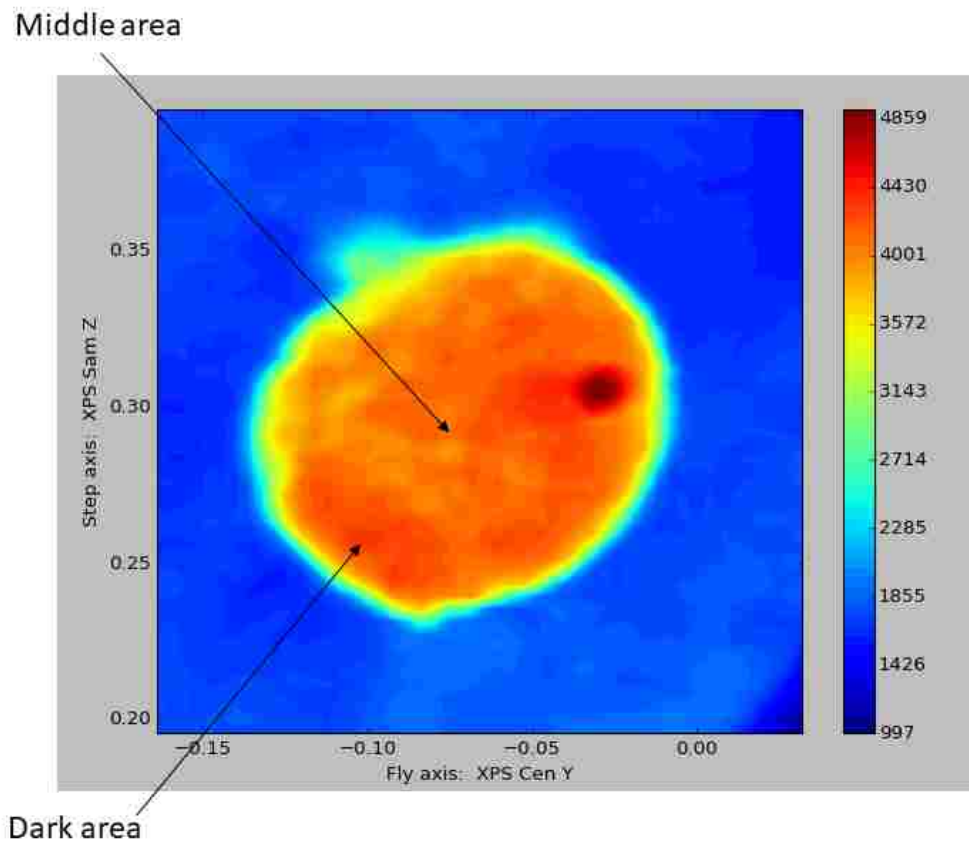


Figure 0-8 X-ray produced 2-D map of unirradiated HgF_2 XeF_2 sample, XRD probed areas are named according to the brightness and the position of obtained image color.

Fig. 5-9 displays the *in situ* XRD patterns obtained at different pressure points as well as XRD patterns of the theoretically predicted at 50 GPa HgF₄ tetragonal crystal structure with *I4/m* space group.

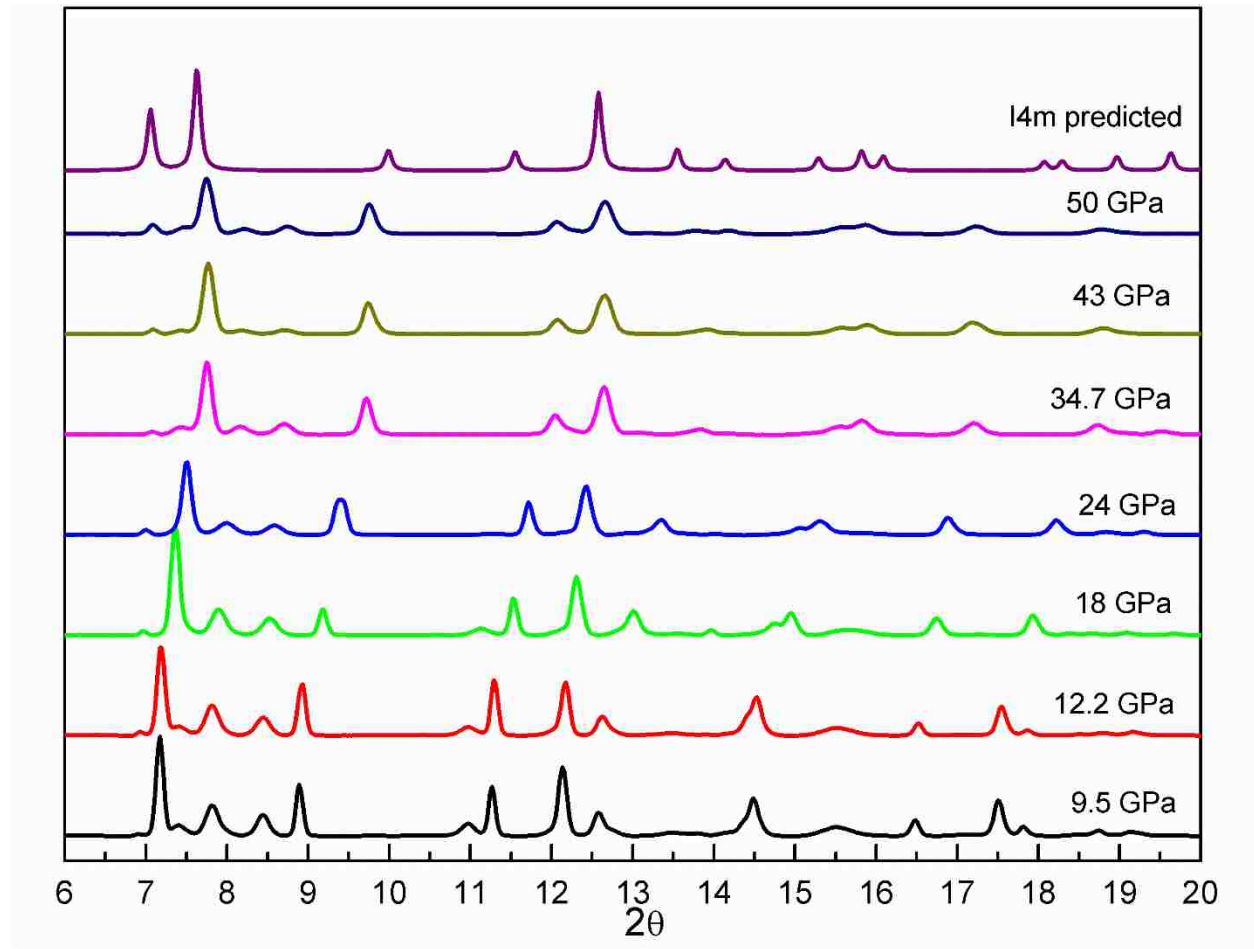


Figure 0-9 XRD patterns of: “dark area” in the unirradiated HgF₂ XeF₂ mixed sample and predicted *I4/m* tetragonal crystal structure of HgF₄.

The XRD pattern obtained at 9.5 GPa clearly demonstrates that “dark area” in the X-ray unirradiated sample contains XeF₂ and high pressure phase of HgF₂ (orthorhombic structures with the space groups *Pnam* and *Pnma*) which is similar to the “average area” in the irradiated sample discussed previously. At a pressure of 50 GPa, the XRD pattern of the “dark area” does not contain any peaks from the predicted HgF₄ crystal structure indicating that for sufficient HgF₄ synthesis higher pressure is required. However, these results support previously discussed results pertaining

to the stability of the high pressure phase of HgF_2 up to 50 GPa and moreover, demonstrate a good agreement with a previously reported study of XeF_2 's high pressure structural behavior[65].

Surprisingly, the same structural behavior is observed for the “middle area” in the

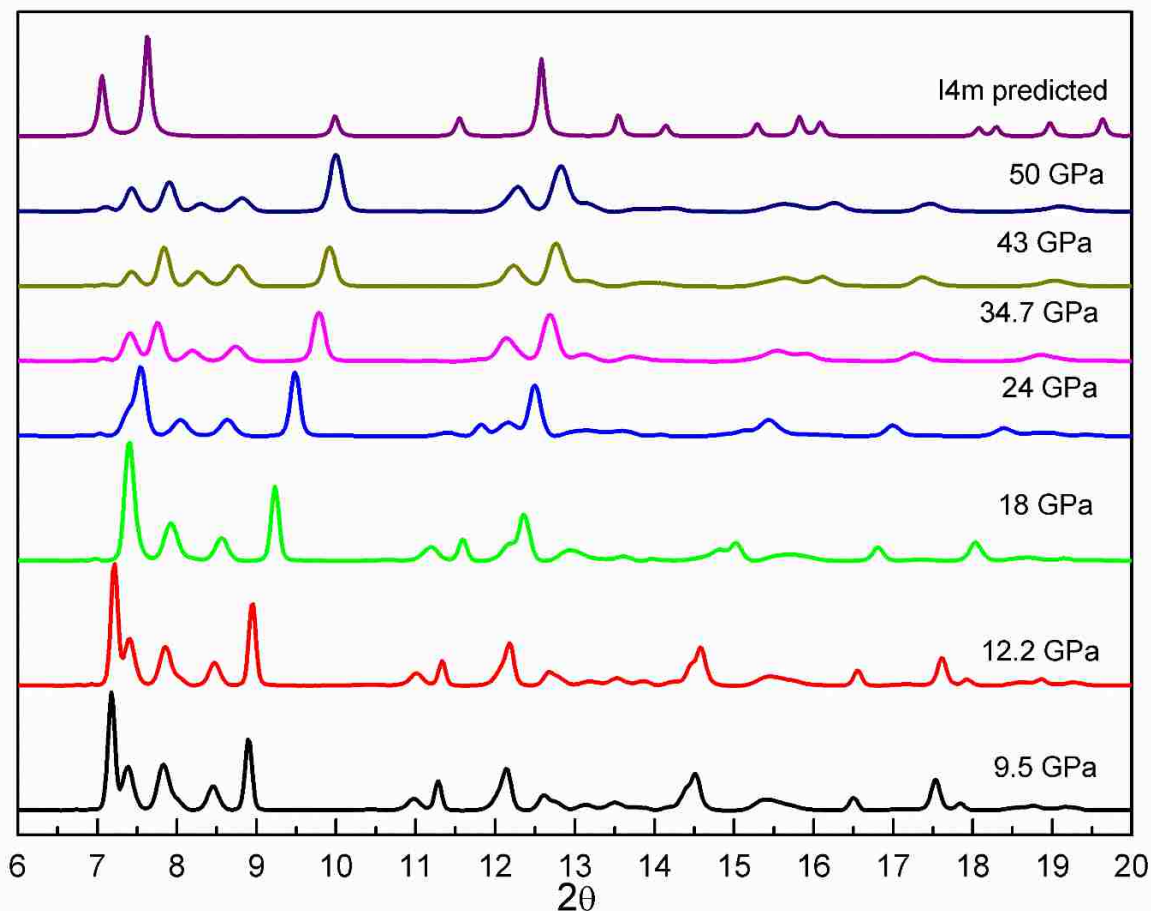


Figure 0-10 XRD patterns of: “middle area” in the unirradiated HgF_2 XeF_2 sample and predicted $I4/m$ tetragonal crystal structure of HgF_4 .

unirradiated HgF_2 XeF_2 sample (see Fig. 5-10). No evidence of HgF_4 presence in the sample pressurized up to 50 GPa is found, nevertheless, as in the previous case the obtained results verify

our studies of the high pressure behavior of HgF_2 and give more insights about the necessary conditions for efficient HgF_4 synthesis at high pressure.

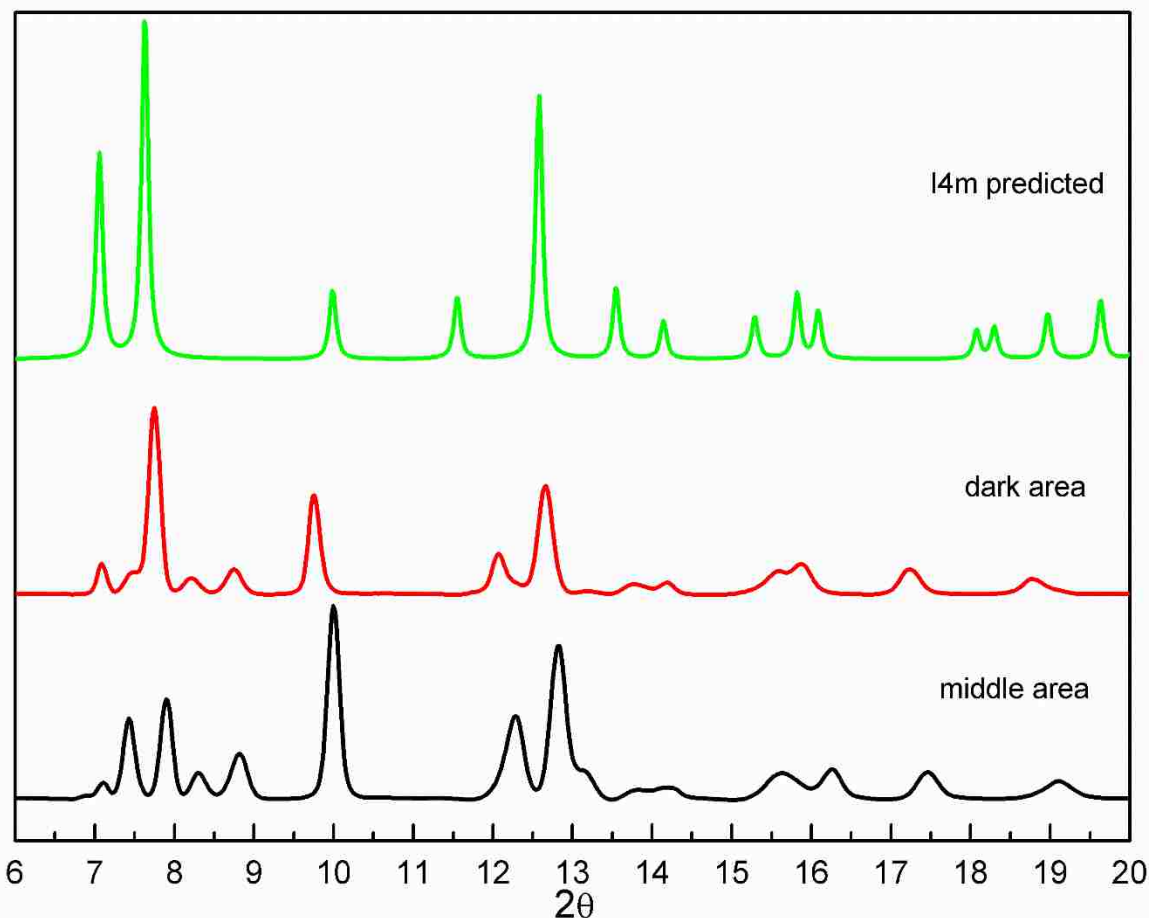


Figure 0-11 XRD patterns comparison of different areas in the unirradiated HgF_2 XeF_2 sample obtained at 50 GPa and predicted tetragonal structure of HgF_4 with the $I4/m$ space group [6].

Finally, we compared the XRD patterns of different areas in the unirradiated HgF_2 XeF_2 sample obtained at 50 GPa (see Fig. 5-11) with the predicted $I4/m$ tetragonal structure of HgF_4 . Although the structural behavior of two areas in the sample shows similar high pressure properties, the differences in the XRD peak intensities suggest different stoichiometric amounts of initial components in the studied spots. Additionally, as in the case of the irradiated sample no peaks which correspond to HgF_4 structure are presented in the XRD patterns obtained at 50 GPa,

indicating that this pressure is not enough for the synthesis of the thermodynamically stable HgF_4 and higher pressure is required for efficient fabrication process.

C. IR characterization of irradiated HgF_2 XeF_2 samples

The irradiated sample of HgF_2 XeF_2 was also characterized by means of synchrotron IR spectroscopy (see Fig. 5-12). Upon the compression no peaks were observed in the 0-19.5 GPa pressure range. However, around 30 GPa two new features appeared near 235 and 474 cm^{-1} respectively. Surprisingly these peaks disappeared when the sample was pressurized above 30 GPa (see Fig. 5-12a). To verify that these two peaks were not due to the experimental setup error, the sample was decompressed from 40 GPa to 32 GPa and compressed again to 35 GPa (see Fig. 5-12b). The same two features were indicated at 235 and 474 cm^{-1} demonstrating that new IR features belong to the studied sample. On pressurizing the sample once again, the features disappeared. We

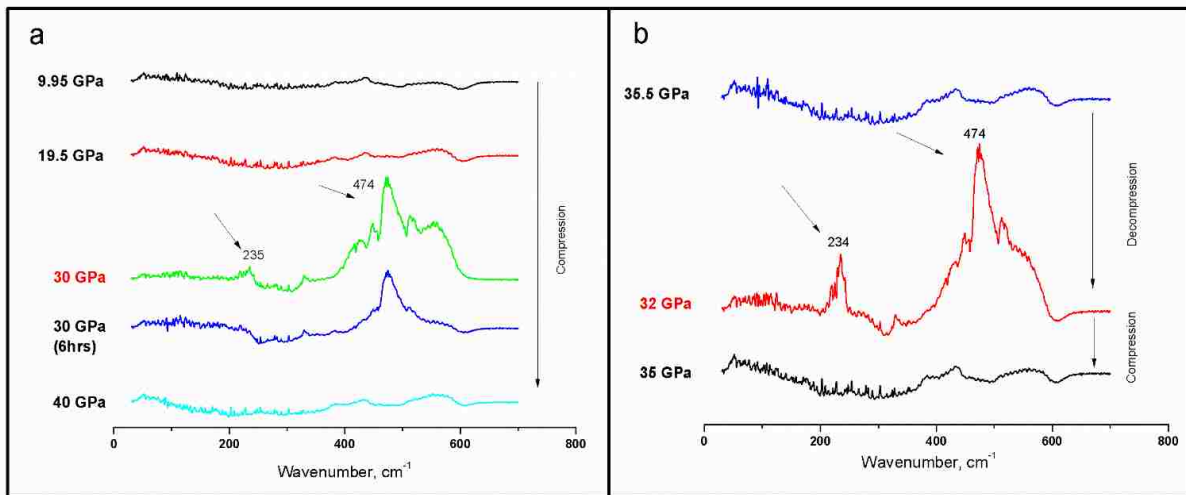


Figure 0-12 Far-IR of the irradiated sample of HgF_2 XeF_2 : (a) upon the compression and (b) compression-decompression around 32 GPa.

suspect that this is due to the diffusion of molecular fluorine toward the edge of the gasket. Upon decompression to ambient pressure, the sample reverted to HgF₂ and residual XeF₂.

Previously, we discussed the high pressure structural behavior of the HgF₂ and XeF₂ samples by means of XRD. It has been found that, in the case of the “dark area” in the irradiated sample, XRD patterns were representing the XeF₂ crystal structure which undergoes phase transition around 29 GPa (see Fig. 5-4). Moreover, previous theoretical studies of high pressure induced structural behavior of XeF₂ suggested the phase transition from *I4/mmm* to *Immm* structure at 31 GPa [65]. Therefore, we propose that changes in IR spectra which occur around 30 GPa (see Fig. 5-12) are due to the chemical/structural transformations of XeF₂. Furthermore, the presence of two new peaks at 235 and 474 cm⁻¹ only around 30 GPa and their disappearance above or below this pressure can be explained by the existence of XeF₂ high-pressure phase transition point at 31 GPa when the system starts to rearrange itself due to the formation of a new structure.

D. Characterization of HgF₂ XeF₂ samples by XAS

The last characterization technique we applied for investigation of high pressure induced HgF₄ synthesis was XAS (see Chapter 3). Fig. 5-13 shows XAS spectra of HgF₂ powder loaded and sealed in capillary, mixture of HgF₂ and XeF₂ pressurized at 50 GPa, and the same mixture irradiated for 4 hours with monochromatic X-rays tuned to Hg L_{α1}-edge which is equal to 9.98 keV. Additionally, the first derivative of all XAS spectra are presented in Fig. 5-13. We found that at 50 GPa pressure the XAS peak which correspond to Hg L-edge (12.283 keV) of mixture sample are shifted at 0.5 eV from the Hg L-edge in HgF₂ in capillary.

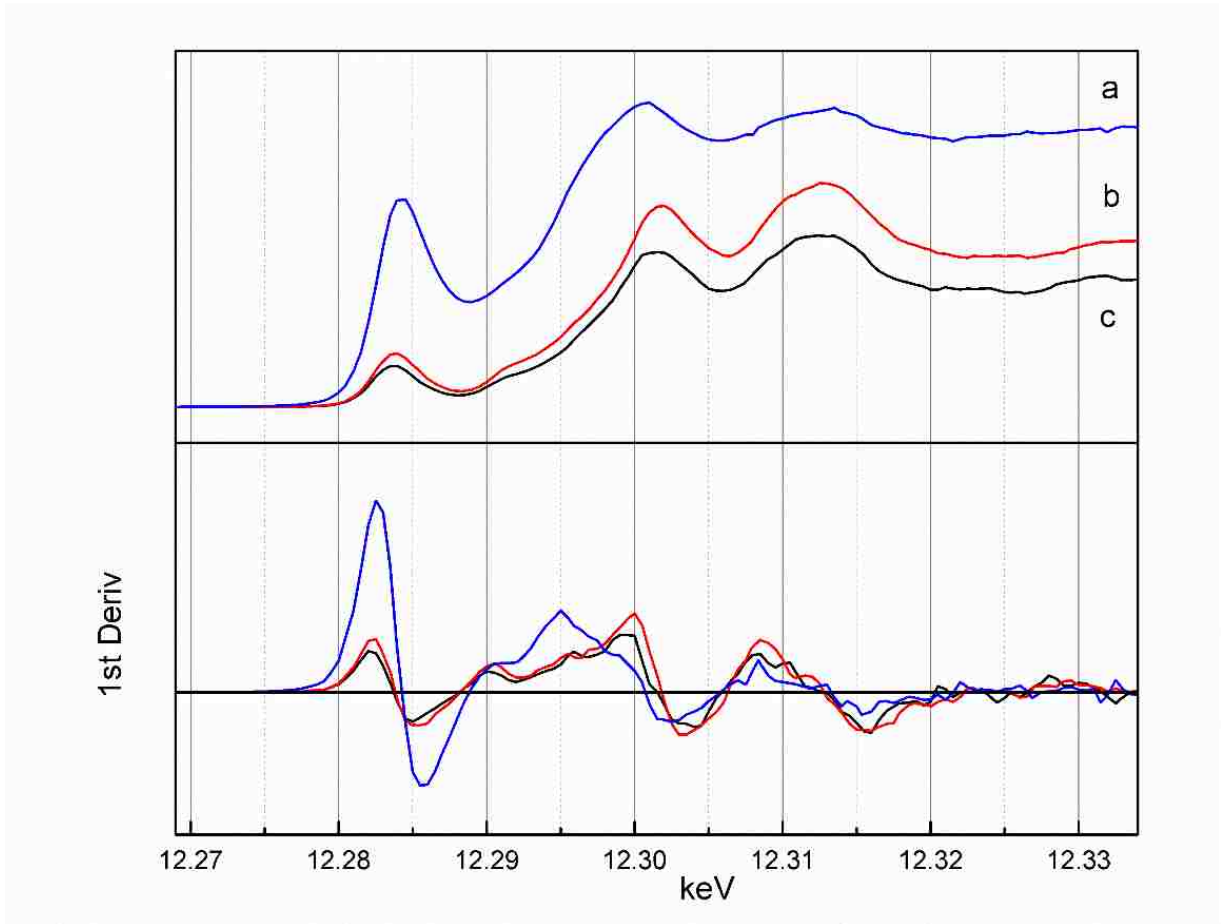


Figure 0-13 X-ray absorption spectra of (Top) (a) HgF₂ loaded in capillary at ambient conditions, (b) mixture of HgF₂ and XeF₂ pressurized at 50 GPa, (c) mixture of HgF₂ and XeF₂ pressurized at 50 GPa and irradiated for 4 hour with X-rays; and the first derivation of the XAS spectra (Bottom).

The shift of 0.5 keV is indicative of the pressure increase from ambient conditions (depicted in Figure 5-13, blue curve) to 50 GPa (red curve) before irradiation. Due to the large flux of X-ray's present at the I-DD beamline at APS, it is possible the sample is already irradiated and decomposed after the initial 30-minute scan at 50 GPa. There is a prominent feature in between 12.29 and 12.30 keV that is not present at 50 GPa it is possible this is suggestive of an electronic transformation within the sample of HgF₂/XeF₂.

E. X-ray induced decomposition of XeF₂

The production of F₂ *in situ* within the DAC was of great interest but due to handling difficulties and inherent toxicity, fluorine was the last stable element with a crystal structure to be determined[71]. Even so, fluorine at high pressures has only been studied experimentally once previously[72] up to 6 GPa. A Raman study (see Chapter 3) was completed to observe changes to the XeF₂ within the sample chamber. Figure 5-12 depicts the white/grey area in the middle of the sample over selected pressure points. The two XeF₂ peaks are observed throughout the pressure range and can be identified based on the assignments in Table 5-1. This is a very different picture

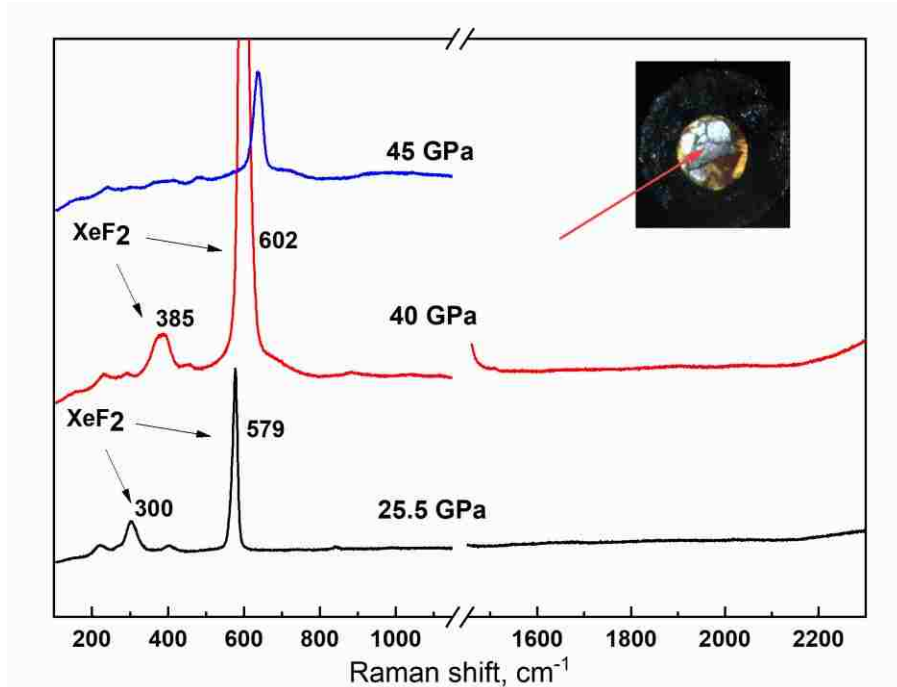


Figure 0-14 Raman spectra at selected pressure points of the white/grey area within the HgF₂/XeF₂ sample. The insert is an image of the sample at 25.5 GPa; two distinct areas are shown within it the white/grey area and the red/yellow area.

from when the yellow-red area (bottom of the sample in the inset of Figure 5-14) is probed. The insert is from the sample described in Figure 5-1 where there was a color change within the sample as pressure increased from yellow (around the edges) to red. The formation of three new peaks is shown in Figure 5-15 specifically around 870 and 1730 cm⁻¹. Niemczyk et al. denoted two experimental found peaks through Raman spectroscopy that belonged to a low temperature (near

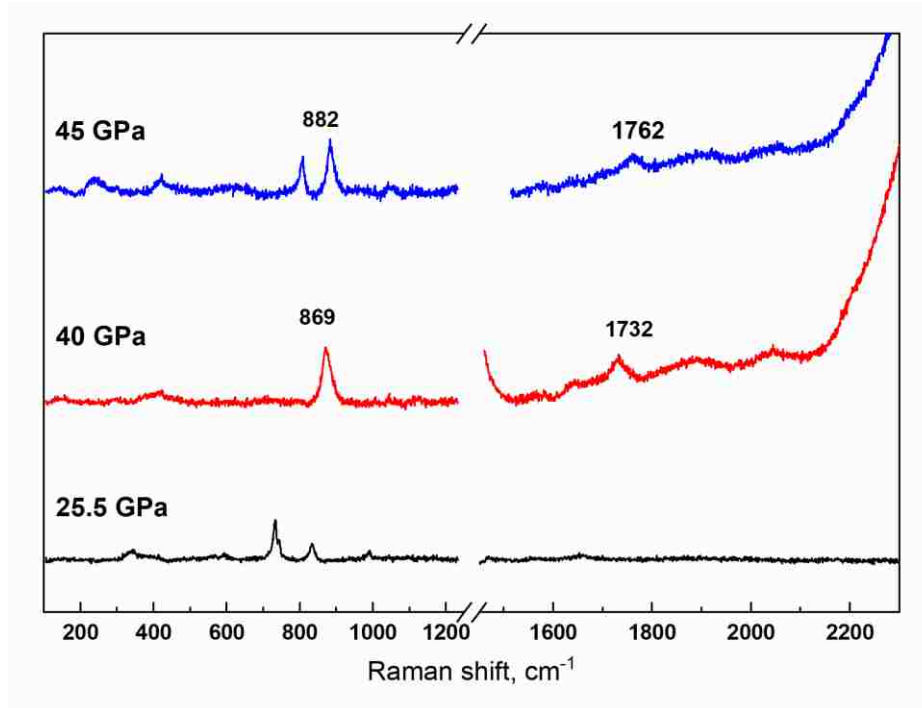


Figure 0-15 Raman spectra of selected pressure points probed on the bottom red/yellow area of the sample.

20 K) where the $\nu(1 - 0)$ is 985 cm^{-1} and the $\nu(2 - 0)$ is at 1764 cm^{-1} [71]. Therefore, there is a possibility of the presence of a solid $\alpha\text{-F}_2$ phase at high pressures within the DAC sample.

Table 0-1 Assignment of XeF_2 peaks based on [65]

Position, cm^{-1}	Assignment
200-300	<i>F</i> wiggle of <i>Xe</i>
550	Stretching <i>F-F</i>

CHAPTER 6: CONCLUSIONS

In this thesis, experimental investigations of the high pressure induced structural behavior of HgF_2 up to 63 GPa and the high pressure synthesis of HgF_4 from HgF_2 in the presence of F_2 has been presented. It is demonstrated that by applying the high pressure ramp technique to the mixture of powdered HgF_2 and crystalline XeF_2 the initial HgF_2 can be purified. The pure HgF_2 exhibits the previously reported cubic structure with $Fm-3m$ space group, and the structural properties of this structure were investigated up to 2.5 GPa. Above 2.5 GPa, a phase transition from cubic to orthorhombic structure was found and by first principle calculations two candidate structures with $Pnma$ and $Pnam$ space groups were proposed. These experiments demonstrated that the high pressure HgF_2 orthorhombic structure is stable up to 63 GPa and reversible (with slight structural hysteresis) to the initial cubic structure upon decompression.

It has been shown that a mixture of X-ray irradiated HgF_2 and XeF_2 (which decomposes into F_2 after irradiation) pressurized does not form an HgF_4 structure, indicating that a pressure of 53 GPa is not enough for the efficient synthesis of the thermodynamically stable HgF_4 . These results also demonstrate a good agreement in our data containing XeF_2 with a previously reported study of XeF_2 high pressure structural behavior.

CHAPTER 7: FUTURE WORK

Many different experiments and investigations have been left for the future due to lack of time (i.e. the experiments require beamtime at national laboratories with a limited timeframe to complete them). The following ideas could be tested:

1. A more in-depth analysis of the structural transition of HgF_2 with pressure via infrared spectroscopy and other vibrational properties of the material.
2. Understanding of the mechanism of HgF_2 purification through the high-pressure ramp process.
3. The mechanism of fluorination needs to be more fleshed out. There were only small signs of the possibility of fluorine inside the sample after X-ray irradiation. While there were apparent decreases in the presence of XeF_2 , spectroscopic probing of the remaining material left much to be desired.
4. The mixture containing HgF_2 + Fluorination agent needs to be taken to higher pressures (above 80 GPa). Due to underestimation in the theory and the presence of nonhydrostatic conditions, the pressure for the transformation from $\text{HgF}_2 + \text{F}_2 \rightarrow \text{HgF}_4$ will be higher than the predicted value.

REFERENCES

- [1] L. Pauling, The nature of the chemical bond—1992, *J. Chem. Educ.* (1992). doi:10.1021/ed069p519.
- [2] M. Miao, J. Botana, M. Pravica, D. Sneed, C. Park, Inner-shell chemistry under high pressure, *Jpn. J. Appl. Phys.* 56 (2017) 05FA10. doi:10.7567/JJAP.56.05FA10.
- [3] X. Wang, Y. Wang, M. Miao, X. Zhong, J. Lv, T. Cui, J. Li, L. Chen, C.J. Pickard, Y. Ma, Cagelike Diamondoid Nitrogen at High Pressures, *Phys. Rev. Lett.* 109 (2012) 175502. doi:10.1103/PhysRevLett.109.175502.
- [4] M.-S. Miao, R. Hoffmann, High Pressure Electrides: A Predictive Chemical and Physical Theory, *Acc. Chem. Res.* 47 (2014) 1311–1317. doi:10.1021/ar4002922.
- [5] M. Miao, Caesium in high oxidation states and as a p-block element, *Nat. Chem.* 5 (2013) 846–852. doi:10.1038/nchem.1754.
- [6] J. Botana, X. Wang, C. Hou, D. Yan, H. Lin, Y. Ma, M. Miao, Mercury under Pressure acts as a Transition Metal: Calculated from First Principles, *Angew. Chemie Int. Ed.* 54 (2015) 9280–9283. doi:10.1002/anie.201503870.
- [7] A.D. McNaught, A. Wilkinson, *IUPAC Compendium of Chemical Terminology: Gold Book*, 2014. doi:http://dx.doi.org/10.1351/goldbook.I03352.
- [8] V. Stumpf, K. Gokhberg, L.S. Cederbaum, The role of metal ions in X-ray-induced photochemistry, *Nat. Chem.* 8 (2016) 237–241. doi:10.1038/nchem.2429.
- [9] K. Gokhberg, P. Kolorenč, A.I. Kuleff, L.S. Cederbaum, Site and energy-selective slow-electron production through intermolecular coulombic decay, *Nature*. (2014).

doi:10.1038/nature12936.

- [10] F. Trinter, M.S. Schöffler, H.K. Kim, F.P. Sturm, K. Cole, N. Neumann, A. Vredenburg, J. Williams, I. Bocharova, R. Guillemin, M. Simon, A. Belkacem, A.L. Landers, T. Weber, H. Schmidt-Böcking, R. Dörner, T. Jahnke, Resonant Auger decay driving intermolecular Coulombic decay in molecular dimers, *Nature*. (2014). doi:10.1038/nature12927.
- [11] H.H. Jawad, D.E. Watt, Physical Mechanism for Inactivation of Metallo-enzymes by Characteristic X-rays, *Int. J. Radiat. Biol. Relat. Stud. Physics, Chem. Med.* 50 (1986) 665–674. doi:10.1080/09553008614551071.
- [12] O. Carugo, K.D. Carugo, When X-rays modify the protein structure: Radiation damage at work, *Trends Biochem. Sci.* (2005). doi:10.1016/j.tibs.2005.02.009.
- [13] D. Goldberger, E. Evlyukhin, P. Cifligu, Y. Wang, M. Pravica, Measurement of the Energy and High-Pressure Dependence of X-ray-Induced Decomposition of Crystalline Strontium Oxalate, *J. Phys. Chem. A.* 121 (2017) 7108–7113. doi:10.1021/acs.jpca.7b05604.
- [14] S. Thürmer, M. Ončák, N. Ottosson, R. Seidel, U. Hergenbahn, S.E. Bradforth, P. Slavíček, B. Winter, On the nature and origin of dicationic, charge-separated species formed in liquid water on X-ray irradiation, *Nat. Chem.* (2013). doi:10.1038/nchem.1680.
- [15] L.S. Cederbaum, J. Zobeley, F. Tarantelli, Giant intermolecular decay and fragmentation of clusters, *Phys. Rev. Lett.* (1997). doi:10.1103/PhysRevLett.79.4778.
- [16] T. Jahnke, Interatomic and intermolecular Coulombic decay: The coming of age story, *J. Phys. B At. Mol. Opt. Phys.* (2015). doi:10.1088/0953-4075/48/8/082001.
- [17] T. Jahnke, H. Sann, T. Havermeier, K. Kreidi, C. Stuck, M. Meckel, M. Schöffler, N.

- Neumann, R. Wallauer, S. Voss, A. Czasch, O. Jagutzki, A. Malakzadeh, F. Afaneh, T. Weber, H. Schmidt-Böcking, R. Dörner, Ultrafast energy transfer between water molecules, *Nat. Phys.* (2010). doi:10.1038/nphys1498.
- [18] J. Zobeley, R. Santra, L.S. Cederbaum, Electronic decay in weakly bound heteroclusters: Energy transfer versus electron transfer, *J. Chem. Phys.* (2001). doi:10.1063/1.1395555.
- [19] O. Marsalek, C.G. Elles, P.A. Pieniazek, E. Pluhaov, J. Vandevondele, S.E. Bradforth, P. Jungwirth, Chasing charge localization and chemical reactivity following photoionization in liquid water, *J. Chem. Phys.* (2011). doi:10.1063/1.3664746.
- [20] O. Svoboda, D. Hollas, M. Ončák, P. Slavíček, Reaction selectivity in an ionized water dimer: Nonadiabatic ab initio dynamics simulations, *Phys. Chem. Chem. Phys.* (2013). doi:10.1039/c3cp51440d.
- [21] P.E. Barran, N.R. Walker, A.J. Stace, Competitive charge transfer reactions in small $[\text{Mg}(\text{H}_2\text{O})\text{N}]^{2+}$ clusters, *J. Chem. Phys.* 112 (2000) 6173. doi:10.1063/1.481218.
- [22] B.A. McGuire, A.M. Burkhardt, S. Kalenskii, C.N. Shingledecker, A.J. Remijan, E. Herbst, M.C. McCarthy, Detection of the aromatic molecule benzonitrile ($c\text{-C}_6\text{H}_5\text{CN}$) in the interstellar medium, *Science* (80-.). (2018). doi:10.1126/science.aao4890.
- [23] M. Pravica, L. Bai, D. Sneed, C. Park, Measurement of the Energy Dependence of X-ray-Induced Decomposition of Potassium Chlorate., *J. Phys. Chem. A.* 117 (2013) 2302–2306. doi:10.1021/jp4008812.
- [24] M. Pravica, E. Evlyukhin, P. Cifligu, B. Harris, J. Jae Koh, N. Chen, Y. Wang, X-ray induced synthesis of a novel material: Stable, doped solid CO at ambient conditions, *Chem.*

- Phys. Lett. 686 (2017) 183–188. doi:10.1016/J.CPLETT.2017.08.053.
- [25] D.M. Applin, M.R.M. Izawa, E.A. Cloutis, D. Goltz, J.R. Johnson, Oxalate minerals on Mars?, *Earth Planet. Sci. Lett.* (2015). doi:10.1016/j.epsl.2015.03.034.
- [26] M. Kaupp, H. Georg Von Schnering, Gaseous Mercury(1v) Fluoride, HgF, : An Ab Initio Study**, n.d. <https://opus.bibliothek.uni-wuerzburg.de/opus4-wuerzburg/frontdoor/deliver/index/docId/5479/file/Kaupp11.pdf> (accessed August 5, 2018).
- [27] X. Wang, L. Andrews, S. Riedel, M. Kaupp, Mercury Is a Transition Metal: The First Experimental Evidence for HgF₄, *Angew. Chemie Int. Ed.* 46 (2007) 8371–8375. doi:10.1002/anie.200703710.
- [28] J.F. Rooms, A. V. Wilson, I. Harvey, A.J. Bridgeman, N.A. Young, Mercury–fluorine interactions: a matrix isolation investigation of Hg···F₂, HgF₂ and HgF₄ in argon matrices, *Phys. Chem. Chem. Phys.* 10 (2008) 4594. doi:10.1039/b805608k.
- [29] S. Riedel, M. Straka, M. Kaupp, Can Weakly Coordinating Anions Stabilize Mercury in Its Oxidation State +IV?, *Chem. - A Eur. J.* 11 (2005) 2743–2755. doi:10.1002/chem.200401130.
- [30] R.L. Deming, A.R. Dahl, A.W. Herlinger, M.O. Kestner, A.L. Allred, Tripositive Mercury. Low Temperature Electrochemical Oxidation of 1,4,8,11-Tetraazacyclotetradecanemercury(II) Tetrafluoroborate, *J. Am. Chem. Soc.* (1976). doi:10.1021/ja00430a020.
- [31] L. Dubrovinsky, N. Dubrovinskaia, E. Bykova, M. Bykov, V. Prakapenka, C. Prescher, K.

- Glazyrin, H.-P. Liermann, M. Hanfland, M. Ekholm, Q. Feng, L. V. Pourovskii, M.I. Katsnelson, J.M. Wills, I.A. Abrikosov, The most incompressible metal osmium at static pressures above 750 gigapascals, *Nature*. 525 (2015) 226–229. doi:10.1038/nature14681.
- [32] W.A. Bassett, Diamond anvil cell, 50th birthday, *High Press. Res.* 29 (2009) 163–186. doi:10.1080/08957950802597239.
- [33] A. Jayaraman, Diamond anvil cell and high-pressure physical investigations, *Rev. Mod. Phys.* 55 (1983) 65–108. doi:10.1103/RevModPhys.55.65.
- [34] R. Hrubiak, S. Sinogeikin, E. Rod, G. Shen, The laser micro-machining system for diamond anvil cell experiments and general precision machining applications at the High Pressure Collaborative Access Team, *Rev. Sci. Instrum.* 86 (2015) 072202. doi:10.1063/1.4926889.
- [35] H.K. Mao, J. Xu, P.M. Bell, Calibration of the ruby pressure gauge to 800 kbar under quasi-hydrostatic conditions, *J. Geophys. Res.* 91 (1986) 4673. doi:10.1029/JB091iB05p04673.
- [36] E. Zarechnaya, The 5-th element. A new high pressure high temperature allotrope, University of Bayreuth, Faculty of Biology, Chemistry and Earth Sciences, 2010. doi:urn:nbn:de:bvb:703-opus-7305.
- [37] K. Takemura, A. Dewaele, Isothermal equation of state for gold with a He-pressure medium, (n.d.). doi:10.1103/PhysRevB.78.104119.
- [38] C. Bortolini, M. Dong, *Synchrotron Radiation Infrared and Raman Spectroscopy for Biomedical Applications*, 2014. <http://www.formatex.info/microscopy6/book/545-556.pdf> (accessed September 16, 2018).
- [39] B. (Barbara H.) Stuart, *Infrared spectroscopy: fundamentals and applications*, J. Wiley,

2004.

- [40] A. Sottile, M. Gysin, *Electronic Absorption Spectroscopy*, (2013).
[http://260h.pbworks.com/w/page-revisions/33532353/Electronic Absorption Spectroscopy](http://260h.pbworks.com/w/page-revisions/33532353/Electronic%20Absorption%20Spectroscopy)
(accessed September 16, 2018).
- [41] P. (Peter J.) Larkin, *Infrared and raman spectroscopy : principles and spectral interpretation*, Elsevier, 2011.
- [42] M. Nazarov, D.Y. Noh, *New generation of europium and terbium activated phosphors : from syntheses to applications*, CRC Press, 2012.
- [43] J. (Jens) Als-Nielsen, D. McMorrow, *Elements of modern X-ray physics*, Wiley, 2011.
<https://www.wiley.com/en-us/Elements+of+Modern+X+ray+Physics%2C+2nd+Edition-p-9780470973943> (accessed September 17, 2018).
- [44] C.J. Humphreys, The significance of Bragg's law in electron diffraction and microscopy, and Bragg's second law, *Acta Crystallogr. Sect. A Found. Crystallogr.* 69 (2013) 45–50.
doi:10.1107/S0108767312047587.
- [45] M. Kunz, A.A. MacDowell, W.A. Caldwell, D. Cambie, R.S. Celestre, E.E. Domning, R.M. Duarte, A.E. Gleason, J.M. Glossinger, N. Kelez, D.W. Plate, T. Yu, J.M. Zaug, H.A. Padmore, R. Jeanloz, A.P. Alivisatos, S.M. Clark, A beamline for high-pressure studies at the Advanced Light Source with a superconducting bending magnet as the source, *J. Synchrotron Radiat.* 12 (2005) 650–658. doi:10.1107/S0909049505020959.
- [46] C. Prescher, V.B. Prakapenka, *DIOPTAS* : a program for reduction of two-dimensional X-ray diffraction data and data exploration, *High Press. Res.* 35 (2015) 223–230.

doi:10.1080/08957959.2015.1059835.

- [47] T.J.B. Holland, S.A.T. Redfern, UNITCELL: A nonlinear least-squares program for cell-parameter refinement implementing regression and deletion diagnostics, *J. Appl. Crystallogr.* (1997). doi:10.1107/S0021889896011673.
- [48] F. Birch, Finite strain isotherm and velocities for single-crystal and polycrystalline NaCl at high pressures and 300°K, *J. Geophys. Res.* 83 (1978) 1257. doi:10.1029/JB083iB03p01257.
- [49] R.J. Angel, M.L. Mazzucchelli, M. Alvaro, F. Nestola, EosFit-Pinc: A simple GUI for host-inclusion elastic thermobarometry, *Am. Mineral.* 102 (2017) 1957–1960. doi:10.2138/am-2017-6190.
- [50] J.A. Van Bokhoven, C. Lamberti, eds., *X-Ray Absorption and X-Ray Emission Spectroscopy*, John Wiley & Sons, Ltd, Chichester, UK, 2016. doi:10.1002/9781118844243.
- [51] J.A. BEARDEN, X-Ray Wavelengths, *Rev. Mod. Phys.* 39 (1967) 78–124. doi:10.1103/RevModPhys.39.78.
- [52] J.E. Penner-Hahn, X-ray Absorption Spectroscopy, in: *Encycl. Life Sci.*, John Wiley & Sons, Ltd, Chichester, UK, 2005. doi:10.1038/npg.els.0002984.
- [53] J.M. Hollas, *Modern Spectroscopy*, 4th Edition, in: *JModern Spectrosc.* 4th Ed., 2005. doi:10.1021/ed082p43.1.
- [54] M.H. Habibi, T.E. Mallouk, Photochemical selective fluorination of organic molecules using mercury (II) fluoride, *J. Fluor. Chem.* 51 (1991) 291–294. doi:10.1016/S0022-

1139(00)80299-7.

- [55] S. Farhadi, P. Zaringhadam, R.Z. Sahamieh, Photolytic decarboxylation of α -arylcarboxylic acids mediated by HgF₂ under a dioxygen atmosphere, *Tetrahedron Lett.* 47 (2006) 1965–1968. doi:10.1016/J.TETLET.2006.01.082.
- [56] K.J. Donald, W.J. Kretz, O. Omorodion, The HgF₂ Ionic Switch: A Triumph of Electrostatics against Relativistic Odds, *Chem. - A Eur. J.* 21 (2015) 16848–16858. doi:10.1002/chem.201502477.
- [57] P. Pyykkö, M. Straka, M. Patzschke, HgH₄ and HgH₆: further candidates for high-valent mercury compounds, *Chem. Commun.* 0 (2002) 1728–1729. doi:10.1039/B203585E.
- [58] M. Kaupp, M. Dolg, H. Stoll, H.G. von Schnering, Oxidation State +IV in Group 12 Chemistry. Ab Initio Study of Zinc(IV), Cadmium(IV), and Mercury(IV) Fluorides, *Inorg. Chem.* 33 (1994) 2122–2131. doi:10.1021/ic00088a012.
- [59] F. Ebert, H. Woitinek, Kristallstrukturen von Fluoriden. II. HgF, HgF₂, CuF und CuF₂, *Zeitschrift Anorg. Und Allg. Chemie.* 210 (1933) 269–272. doi:10.1002/zaac.19332100307.
- [60] M. Hostettler, D. Schwarzenbach, Phase diagrams and structures of HgX₂ (X = I, Br, Cl, F), *C. R. Chim.* 8 (2004). doi:10.1016/j.crci.2004.06.006.
- [61] X. Wang, J. Li, The new phase of HgF₂ at high pressure, *EPL (Europhysics Lett.)* 102 (2013) 36002. doi:10.1209/0295-5075/102/36002.
- [62] S. Stavber, T. Sotler, M. Zupan, A. Popovic, Fluorination with XeF₂. Part 40. The Important Role of π -Bond Disruption in Fluorine Addition to Phenyl-Substituted Alkenes, *J. Org.*

- Chem. 59 (1994) 5891–5894. doi:10.1021/jo00099a015.
- [63] A. Tarditi, P. Kondratyuk, P.K. Wong, A.J. Gellman, Controlling the work function of a diamond-like carbon surface by fluorination with XeF₂, *J. Vac. Sci. Technol. A Vacuum, Surfaces, Film.* 28 (2010) 1250–1254. doi:10.1116/1.3480335.
- [64] E. Evlyukhin, L. Museur, M. Traore, C. Perruchot, A. Zerr, A. Kanaev, A New Route for High-Purity Organic Materials: High-Pressure-Ramp-Induced Ultrafast Polymerization of 2-(Hydroxyethyl)Methacrylate, *Sci. Rep.* 5 (2016) 18244. doi:10.1038/srep18244.
- [65] G. Wu, X. Huang, Y. Huang, L. Pan, F. Li, X. Li, M. Liu, B. Liu, T. Cui, Confirmation of the Structural Phase Transitions in XeF₂ under High Pressure, *J. Phys. Chem. C.* 121 (2017) 6264–6271. doi:10.1021/acs.jpcc.6b11558.
- [66] M. Tramšek, B. Žemva, Synthesis, properties and chemistry of xenon (II) fluoride, *Acta Chim. Slov.* 53 (2006) 105–116. doi:10.1002/chin.200721209.
- [67] S. Torabi, L. Hammerschmidt, E. Voloshina, B. Paulus, *Ab initio* investigation of ground-state properties of group-12 fluorides, *Int. J. Quantum Chem.* 114 (2014) 943–951. doi:10.1002/qua.24695.
- [68] E. Cadelano, G. Cappellini, Electronic structure of fluorides: general trends for ground and excited state properties, *Eur. Phys. J. B.* 81 (2011) 115–120. doi:10.1140/epjb/e2011-10382-1.
- [69] T. Taniguchi, T. Sato, W. Utsumi, T. Kikegawa, O. Shimomura, Effect of nonhydrostaticity on the pressure induced phase transformation of rhombohedral boron nitride, *Appl. Phys. Lett.* 70 (1997) 2392–2394. doi:10.1063/1.118882.

- [70] D. Duan, X. Jin, Y. Ma, T. Cui, B. Liu, G. Zou, Effect of nonhydrostatic pressure on superconductivity of monatomic iodine: An *ab initio* study, Phys. Rev. B. 79 (2009) 064518. doi:10.1103/PhysRevB.79.064518.
- [71] T.M. Niemczyk, R.R. Getty, G.E. Leroi, Solid Fluorine and Solid Chlorine: Crystal Structures and Intermolecular Forces The, Cryst. Struct. α -Fluorine J. Chem. Phys. 59 (1973) 4890. doi:10.1063/1.1679912.
- [72] D. Schiferl, S. Kinkead, R.C. Hanson, D.A. Pinnick, Raman spectra and phase diagram of fluorine at pressures up to 6 GPa and temperatures between 10 and 320 K, J. Chem. Phys. 87 (1987) 64502. doi:10.1063/1.453700.

CURRICULUM VITAE

Sarah Schvck

✉ s.schvck@gmail.com
🏠 Department of Physics and Astronomy
University of Nevada, Las Vegas
Las Vegas, NV 89154-4002

Education

- 2016 – current **■ M.Sc. in Physics, University of Nevada, Las Vegas, U.S.**
Working Thesis title: *Studies of Inner-shell Chemistry of Mercury Based Compounds under Extreme Conditions.*
Advisor: Prof. Michael Pravica.
- 2012 – 2015 **■ B.S. in Physics, University of Georgia, U.S.**
Projects: *Effect of Organic Hole Scavengers on the Photochromism of Bi₂WO₆ and Growth of Cu nanofilms on polystyrene bead mono layer substrates by means of oblique angle physical vapor deposition.*
Advisor: Prof. Yiping Zhao.

Internships

- May – July 2016 **■ LSE Intern at Savannah River National Lab**
- Jan – April 2016 **■ ORAU Intern at Savannah River National Lab**
Synthesis of noble metal nanoparticles and characterization of their size and surface charge. Study of nucleation mechanism of noble metal nanoparticle growth on oxide-based nanoparticles.

Synchrotron Experimental Research

- Argonne National Laboratory **■ Advanced Photon Source, Sector 16 HPCAT. Beamlines: ID-D, ID-B, BM-D, and BM-B.**
- University of Saskatchewan **■ Canadian Light Source. Beamlines: Far-IR (02B1-1) and Mid-IR (01B1-1).**
- Lawrence Berkeley National Laboratory **■ Advanced Light Source. Beamline: BL 12.2.2.**
- Total Experimental Hours **■ >900**

Teaching Experience

- 2017 – current **■ Graduate Teaching Assistant at University of Nevada, Las Vegas, U.S.**
Two introductory physics laboratory sections per semester: non-calculus based physics I and calculus based electromagnetism.

Skills

- Investigation of X-ray induced chemical reactions under ambient and extreme conditions.
- Diamond anvil cell (DAC), multi-anvil large volume press, Paris Edinburg Cells (PEC). Proficiency in handling Beryllium gaskets.
- Characterization of materials by means of Raman, Far-IR, Mid-IR, FTIR, UV-Vis spectroscopy, XRD, XAS, XANES, XRS, and EDXRD.

Skills (continued)

- Synthesis of nanomaterials: (i) oblique angle co-deposition, (ii) electron beam deposition, and (iii) vacuum dual-source magnetron sputtering deposition.
- Characterization of nanomaterials by means of Scanning electron microscopy (SEM)
- Preparation of colloid polystyrene bead monolayers using an air-water interface self-assembly process.
- Lithography: (i) experience in a Class 100 clean room, (ii) photoresist epoxy coating of substrate, and (iii) soft baking and UV exposure.

Research Publications

Journal Articles

- 1 Evlyukhin, E., Kim, E., Goldberger, D., Cifligu, P., Schyck, S., Weck, P. F. & Pravica, M. (2018). High-pressure-assisted x-ray-induced damage as a new route for chemical and structural synthesis. *Phys. Chem. Chem. Phys.* 20, 18949–18956. doi:10.1039/C8CP02119H

International Conferences

- 2018 ■ **Stewardship Science Academic Programs (SSAP)** Poster presented:
S. Schyck, E. Evlyukhin, P. Cifligu, B. Harris, D. Goldberger, M. Pravica. "*Application of Useful Hard X-Ray Photochemistry for the Synthesis of Mercury (IV) Fluoride*," SSAP Symposium 2018 (21–22 February 2018, Rockville, Maryland, US).
- 2017 ■ **SSAP** Poster Presented:
S. Schyck, D. Sneed, E. Evlyukhin, Y. Wang, M. Pravica. "*High Pressure Studies of HgF₂*," SSAP Symposium 2017 (12–13 April 2017, Chicago, USA).
- 2015 ■ **APS conference for Undergraduate Women in Physics (CUWiP)** Held at the North Carolina Research Triangle on the 16–18 of January, 2015.
- 2013 ■ **Southeast Conference for Undergraduate Women in Physics (CUWiP)** Held at the University of Central Florida on the 18–20 of January, 2013.

References

Available on Request